

1 **Observations of creep of polar firn at different temperatures**

2

3 Yuan Li^{1,3}, Kaitlin Keegan², Ian Baker¹

4 ¹Thayer School of Engineering, Dartmouth College, Hanover, NH, 03755, USA

5 ²Department of Geological Sciences & Engineering, University of Nevada, Reno, Reno, NV,

6 89557, USA

7 ³X-Here (Future ice-based Hydrogen energy & resilient environments) Trek Laboratory

8 (Establishing), Howard Beach, NY, 11414, USA

9 *Correspondence to:* Ian Baker (ian.baker@dartmouth.edu)

10 **Abstract**

11 To improve our understanding of firn compaction and deformation processes, constant-load
12 compressive creep tests were performed on specimens from a Summit, Greenland ($72^{\circ}35' N$,
13 $38^{\circ}25' W$) firn core that was extracted in June, 2017. Cylindrical specimens were tested at
14 temperatures of $-5^{\circ}C$, $-18^{\circ}C$ and $-30^{\circ}C$ from depths of 20 m, 40 m and 60 m at stresses of 0.21
15 MPa, 0.32 MPa and 0.43 MPa, respectively. The microstructures were characterized before and
16 after creep using both X-ray micro-computed tomography (micro-CT) and thin sections viewed
17 between optical crossed polarizers. The results of these experiments comprise a novel data set on
18 the creep of firn at three depths of a firn column at three different temperatures, providing useful
19 calibration data for firn model development. Examining the resulting strain vs. time and strain vs.
20 strain rate curves from the creep tests revealed the following notable features. First, the time
21 exponent k was found to be 0.34–0.69 during transient creep, which is greater than the 0.33
22 usually observed in fully-dense ice. Second, the strain rate minimum (SRmin) in secondary creep
23 occurred at a greater strain from specimens with lower density and at higher temperatures. Third,
24 tertiary creep occurred more easily for the lower-density specimens at greater effective stresses
25 and higher temperatures, where strain softening is primarily due to recrystallization. Fourth, the
26 SRmin is a function of the temperature for a given firn density. Lastly, we developed empirical
27 equations for inferring the SRmin, as it is difficult to measure during creep at low temperatures.
28 The creep behaviors of polar firn, being essentially different from full-density ice, imply that firn
29 densification is an indispensable process within the snow-to-ice transition, particularly firn
30 deformation at different temperatures connected to a changing climate.

31

32 **Keywords:** Firn densification; Creep; Activation energy; Cryospheric micro-CT; Temperature

33 **1. Introduction**

34 Understanding firn compaction and densification experimentally is critical for developing
35 physics-based firn models that are necessary for many glaciological applications. For example,
36 such models are essential for reconstructing ice-core paleoclimate records by simulating the
37 lock-in depth of gases and the smoothing of climate signals (Schwander et al., 1997; Goujon et al.,
38 2003). They are also crucial for interpreting ice-mass changes from satellite altimetry data, as
39 they allow for the accurate correction of firn air content and surface elevation changes not related
40 to underlying ice dynamics (Ligtenberg et al., 2011; Simonsen et al., 2013). However, the firn
41 models used for these applications are empirical and are known to perform poorly outside of their
42 calibration range (Lundin et al., 2017). Thus, a better understanding of firn compaction is
43 necessary to refine firn models for these important glaciological applications. Laboratory
44 compressive experiments on firn and ice improve our understanding of their respective flow laws
45 and advance the development of firn models under a range of conditions. The rheology of
46 polycrystalline ice, particularly its temperature-dependent creep deformation, is a cornerstone of
47 glaciological modeling. Numerous studies have established a robust framework for understanding
48 ice deformation, primarily through laboratory creep experiments (e.g. Glen, 1955; Weertman,
49 1983; Budd and Jacka, 1989; Durham et al., 2001; Goldsby and Kohlstedt, 2001; Petrenko and
50 Whitworth, 1999). This body of work has confirmed that ice creep is strongly governed by
51 temperature, typically described by an Arrhenius relationship with a well-constrained activation
52 energy for grain-scale processes like dislocation glide and climb (e.g. Jacka, 1984; Hooke, 2005).
53 In contrast, the mechanical behavior of firn, the intermediate porous material between snow and
54 glacial ice, remains comparatively poorly characterized, especially with respect to temperature.

55 The experimental observations are interpreted by drawing parallels between firn deformation and
56 the mechanical properties of its constituent material, polycrystalline ice. This connection is
57 formalized through a poromechanics approach, where the behavior of the porous firn is derived
58 from that of the ice skeleton using continuum mechanics and homogenization principles
59 (Scapozza and Bartelt, 2003; Gagliardini and Meyssonier, 2000; Coussy, 2004; Hutter and Johnk,
60 2004; Srivastava et al., 2010; Theile et al., 2011). While numerous studies have investigated ice
61 deformation (e.g. Steinemann, 1954; Maeno and Ebinuma, 1983; Li et al., 1996; Jacka and Li,
62 2000; Song et al., 2006a, 2006b, 2008; Treverrow et al., 2012; Hammonds and Baker, 2016, 2018)
63 and firn deformation (e.g. Landauer, 1958; Mellor, 1975; Salm, 1982; Ambach and Eisner, 1985;
64 Meussen et al., 1999; Bartelt and von Moos, 2000; Theile et al., 2011; Li and Baker, 2021, 2022a),
65 existing firn data are sparse and fragmented. A critical knowledge gap persists in the systematic
66 experimental quantification of firn's mechanical response across a broad range of temperatures.
67 Temperature is a first-order control on firn densification and deformation rates, yet most
68 laboratory studies have been conducted at a limited number of isothermal conditions, often
69 focused on a single density or at temperatures near the melting point (e.g. Mellor, 1975; Maeno
70 and Ebinuma, 1983). Consequently, there is a pronounced lack of experimental data necessary to
71 derive the systematic activation energy for the creep of firn over its full density spectrum. This
72 parameter is not merely a scalar but is likely a function of density, microstructure, and the
73 dominant deformation mechanism (compaction versus shear), transitioning from grain-boundary
74 sliding in low-density firn to dislocation creep in high-density firn and ice (Hammonds and Baker,
75 2018; Li, 2022; Li and Baker, 2022a). The absence of comprehensive, temperature-variable creep
76 data for firn across its density range renders it insufficient for constraining the

77 temperature-dependence terms in modern, physics-based firn models. Our work fills this gap via
78 X-ray micro-computed tomography-analyzed mechanical examinations, e.g. a systematic series of
79 constant-stress creep experiments on firn cores of varying density, conducted across a thermally
80 controlled range from -30°C to -5°C . This allows for the direct determination whether the
81 apparent activation energy is a function of density, thereby providing the essential experimental
82 foundation needed to improve predictions of firn densification in ice-sheet and glacier models.
83 Notably, the mechanical behavior of two-phase flow coupling the airflow with the ice matrix
84 deformation has not yet been performed experimentally hitherto, even though the role of the
85 microstructures of firn on airflow has been studied (Albert et al., 2000; Courville et al., 2010;
86 Adolph and Albert, 2014). This difficulty is largely due to the limitations of the observation
87 techniques of nondestructive visualization of the microstructures during snow and firn
88 deformation. Thus, caution should be taken when extending the conclusions to ice sheet and
89 glacier scales from sample laboratory experiments. Macroscopically, the creep of firn obeys a
90 power-law dependence of the strain rate on the stress at constant stresses and temperature, similar
91 to that of full-density ice (Li and Baker, 2022a). Note that both the diffusivity and permeability of
92 the air in the pores (Albert et al., 2000; Courville et al., 2010; Adolph and Albert, 2014) impact
93 heat conduction of the ice matrix, and hence the grain growth. This is tightly tied to the
94 micro-mechanisms, e.g. grain-boundary and lattice diffusion of the ice crystals (Li and Baker,
95 2021), superplastic deformation and inter-particle sliding from dislocation motion in the ice necks
96 (Bartelt and Von Moos, 2000), and likely rearrangement of the ice particles (Perutz and Seligman,
97 1939; Anderson and Benson, 1963; Ebinuma and Maeno, 1987).

98

99 Through experiments on isotropic ice samples subjected to uni-axial compaction at octahedral
100 stresses of 0.1–0.8 MPa and temperatures from -45°C to -5°C , Jacka and Li (2000) determined
101 the mechanisms involved in the empirical *power-law flow*, which was derived by Glen (1955) for
102 stresses ranging from 0.1–1 MPa at temperatures spanning from -13°C to the melting-point. They
103 found that dynamic recrystallization predominated at higher temperatures and stresses, whereas
104 crystal rotation governed at lower temperatures and stresses. Later, Goldsby and Kohstedt (2001)
105 found that ice could exhibit *superplastic flow*, which depends inversely on the grain size,
106 particularly for fine-grained ice, while both dislocation creep and basal slip-limited creep were
107 unrelated to the grain size at stresses of 0.1 MPa or less over a wide range of temperatures.
108 Moreover, Baker and Gerberich (1979) reported that the apparent activation energy for creep for
109 polycrystalline ice, which was derived from tests at constant stress and temperatures ranging from
110 -40°C to -5°C , increased with increasing volume fraction of inclusions (bubbles, impurities, dust,
111 and air clathrate hydrates). Such inclusions governed the evolution of grain size related to thermal
112 activations. The activation energies for the creep of snow and ice have been determined by a
113 number of authors, and values ranging from 58.6–113 kJ mol^{-1} were obtained under both uniaxial
114 and hydrostatic experiments for snow with a density of $\sim 400 \text{ kg m}^{-3}$ at -13.6°C to -3.6°C
115 (Landauer, 1958); 44.8–74.5 kJ mol^{-1} from snow with densities of 440–830 kg m^{-3} at -34.5°C to $-$
116 0.5°C (Mellor and Smith, 1966); $\sim 72.9 \text{ kJ mol}^{-1}$ for firn with a density of 320–650 kg m^{-3} at the
117 South Pole (Gow, 1969); $69 \pm 5 \text{ kJ mol}^{-1}$ for a mean snow density of $423 \pm 8 \text{ kg m}^{-3}$ at -19°C to
118 -11°C (Scapozza and Bartelt, 2003); the 78 kJ mol^{-1} from polycrystalline ice compression
119 deformation at a temperature of -10°C (Duval and Ashby, 1983); $\sim 60 \text{ kJ mol}^{-1}$ for artificial and
120 natural ice at the South Pole (Pimienta and Duval, 1987); and $78 \pm 4 \text{ kJ mol}^{-1}$ for monocrystal ice

121 at -20°C to -4.5°C and $75 \pm 2 \text{ kJ mol}^{-1}$ for bicrystal ice at -15°C to -4.5°C (Homer and Glen,
122 1978). In summary, the flow law of polycrystalline ice and firn depends on the effects of
123 recrystallization, grain size, inclusions (Mellor and Testa, 1969; Vickers and Greenfield, 1968;
124 Barnes et al., 1971; Baker and Gerberich, 1979; Goodman et al., 1981), and the temperature.

125

126 With advanced observation techniques, the relevant microstructural parameters of snow and firn
127 have been characterized by a number of scientists (Arnaud et al., 1998; Coleou et al., 2001; Flin et
128 al., 2004; Wang and Baker, 2013; Wiese and Schneebeli, 2017; Li, 2022). Using X-ray
129 micro-computed tomography (micro-CT), Li and Baker (2022b) characterized metamorphism
130 from snow to depth hoar under opposing temperature gradients. Only rarely has work been
131 performed on the co-effects of temperature and stress on the densification of firn while
132 simultaneously visualizing the microstructural changes using a micro-CT. For example, Schleef et
133 al. (2014) reported that densification under varying conditions of overburden stress and
134 temperature from natural and laboratory-grown new snow showed a linear relationship between
135 density and the specific surface area (SSA). To this end, the aim of our present work is to
136 investigate the temperature dependence of the creep of polar firn and relate this to the change of
137 microstructure determined using micro-CT studies on firn obtained from Summit, Greenland in
138 2017. As is well known, temperature is a key parameter affecting the flow of firn and ice, and
139 plays a determined role in their deformation, especially for polythermal and temperate glaciers.
140 Due to the great difficulty of analyzing firn and ice deformation with the presence of liquid water,
141 this work focuses on the firn creep from the dry snow zone, i.e., areas without meltwater, at
142 different temperatures.

143

144 **2. Samples and measurements**

145 *2.1 Samples*

146 Three cylindrical samples (22 ± 0.5 mm diameter; 50 ± 0.5 mm high) were produced at each of
147 three depths of 20 m, 40 m and 60 m from the same 2017 Summit, Greenland firn core that was
148 studied in Li and Baker (2022a). Both the densities and porosities of these above samples are
149 typical of values in the snow-to-ice transition zone as introduced in Section 1. It is important to
150 note that the reduction in effective stress with increasing depth is evident in samples taken from
151 these three specified depths (**Appendix A**). Before creep testing, one cylindrical firn samples
152 from each depth was stored at a temperature of $-5 \pm 0.5^\circ\text{C}$, $-18 \pm 0.5^\circ\text{C}$, and $-30 \pm 0.5^\circ\text{C}$ for two
153 days to achieve thermal equilibrium (Li and Baker, 2022a). It's also important to note that firn is a
154 heterogeneous material that can have variations in layering, fabric, grain size, and impurity
155 concentration across short distances. Thus, care was taken to extract the three replicate samples
156 from the core at each depth as closely as possible to reduce the variability in their initial
157 conditions.

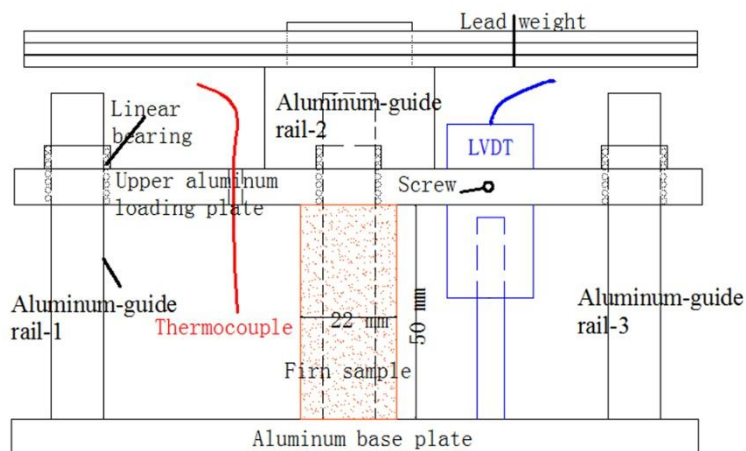
158

159 *2.2 Creep measurements*

160 Three home-built creep jigs were placed in individual Styrofoam boxes in three different cold
161 rooms that were held at temperatures of $-5 \pm 0.5^\circ\text{C}$, $-18 \pm 0.5^\circ\text{C}$ and $-30 \pm 0.5^\circ\text{C}$. Each creep jig
162 consists of an aluminum base plate and three polished aluminum-guide rails passing through
163 linear bearings that hold the upper aluminum loading plate (**Figure 1**). A linear voltage
164 differential transducer (LVDT-Omega LD-320: resolution of 0.025%; linearity error of $\pm 0.15\%$

165 of full-scale output), parallel to the three aluminum-guide rails, was located adjacent to the center
166 of the upper plate, and fixed firmly using a screw through the plate (**Figure 1**) for measuring the
167 displacement during a test. The displacement was logged every 5 seconds using a Grant SQ2010
168 datalogger (accuracy of 0.1%). Temperatures were logged at 300-second time intervals over the
169 entire test period, using a k-type thermocouple (Omega RDXL4SD thermistor: resolution of 0.1°C)
170 that was mounted inside each box. In this work, specimens were tested at temperatures of $-5 \pm$
171 0.2°C , $-18 \pm 0.2^{\circ}\text{C}$ and $-30 \pm 0.2^{\circ}\text{C}$ from depths of 20 m (applied stress 0.21 MPa), 40 m (0.32
172 MPa) and 60 m (0.43 MPa). There are smaller error bars for the temperature of the specimens
173 than the room temperature because the creep jigs were in insulated Styrofoam boxes. The stresses
174 were chosen based on experience from previous tests (Li and Baker, 2022a) in order to give
175 measurable creep rates in a reasonable time.

176



177

178 **Figure 1:** Schematic illustrating the home-built compressive creep jigs. More details can be found
179 in (Li & Baker, 2022a).

180

181

182 2.3 *X-ray micro-computed tomography (micro-CT)*

183 Each specimen at each depth and temperature combination was scanned using a Skyscan 1172
184 micro-CT, before and after creep testing. Each micro-CT scan lasted ~2 h. The cubic Volume of
185 Interest (VOI, a side length of 8 mm) was taken from near the center of the firn specimen as
186 conducted in Li and Baker (2022a). The microstructural parameters obtained from the micro-CT
187 data are the SSA, the mean structure thickness of the ice matrix (S.Th), the area-equivalent circle
188 diameter of the pores (ECDa), the total porosity (TP), the closed porosity (CP), and the structure
189 model index (SMI). The SSA (mm^{-1}) is the ratio of the ice surface area to total firn volume (ice
190 plus air) in a VOI analytical element, and is calculated using the hexahedral marching cubes
191 algorithm via CTAn software (Wang and Baker, 2013). It characterizes the thickness and
192 complexity of the firn microstructure. Changes in SSA indicate a change in free energy of the ice
193 surfaces, the decrease of which represents the occurrence of sintering-pressure. The S.Th (mm) is
194 the mean structure thickness of an ice matrix (Hildebrand and Ruegsegger, 1997), which
195 represents the characteristic size of an ice particle in the firn, where the ice particle consists of one
196 or many crystals or grains. It is measured based on the largest sphere diameter that encloses a
197 point in the ice matrix and is completely bounded within solid surfaces. The ECDA (mm) is the
198 diameter of a circle having the same area as the average for all pores in the VOI from the 2-D
199 binary images, indicative of the characteristic size for the void space (Adolph and Albert, 2014).
200 The TP (%) is the ratio of the pore volume, including both open and closed pores, to the total VOI.
201 The CP (%) is the ratio of the volume of the closed pores to the total volume of solid plus closed
202 pores volume in a VOI, while the open porosity (%) is the ratio of the volume of the open pores to
203 the total VOI. The SMI is calculated based on the dilation of a 3-D voxel model (Hildebrand and

204 Ruegsegger, 1997) $SMI = 6(S' \times V)/S^2$, where S' is the change in the surface area due to
205 dilation, and V and S are the object volume and surface area, respectively. It indicates the
206 prevalent ice curvature, negative values of which represent a concave surface, e.g. the hollow air
207 structure surrounded by an ice matrix. The more negative the SMI value, the more spherical the
208 pore. Notably, the micro-CT-derived density of each specimen agrees well with the bulk density
209 measured using the mass-volume approach (Li and Baker, 2021).

210

211 *2.4 Thin section preparation and imaging*

212 Thin sections for optical photographs before and after creep testing were cut from bulk specimens,
213 one side of which was first smoothed with a microtome. This side was then frozen onto a glass
214 plate ($100 \times 60 \times 2$ mm) by dropping supercooled gas-free water along its edges. Its thickness
215 was reduced to ~ 2 mm by a band saw, and finally thinned further to a uniform thickness of ~ 0.5
216 mm using a microtome. Images were captured using a digital camera after each thin section was
217 placed on a light table between a pair of crossed polarizing sheets.

218

219 **3 Results and discussion**

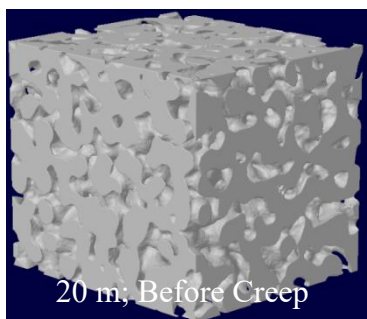
220 *3.1 Microstructures before creep*

221 Increasing firn density with increasing depth from either of the -5°C , -18°C , and -30°C
222 specimens can be readily recognized by visual inspection of the micro-CT 3-D reconstructions of
223 the firn microstructure (**Figure 2**). Correspondingly, the microstructural parameters, with the
224 exception of the CP, changed monotonically with increasing depth at each temperature, e.g. the $-$
225 30°C samples increased in density from $591 \pm 1.4 \text{ kg m}^{-3}$, to $683 \pm 4.2 \text{ kg m}^{-3}$, to $782 \pm 1.5 \text{ kg m}^{-3}$,

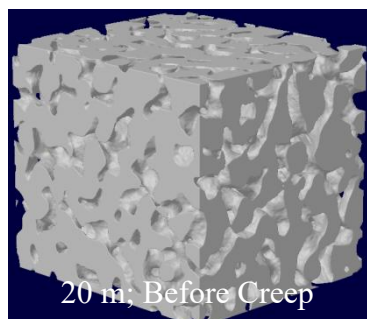
226 decreased in SSA from $4.64 \pm 0.04 \text{ mm}^{-1}$, to $3.3 \pm 0.06 \text{ mm}^{-1}$, to $2.39 \pm 0.01 \text{ mm}^{-1}$, and decreased
227 in TP from $35.6 \pm 0.05\%$, $25.6 \pm 0.4\%$, to $14.8 \pm 0.2\%$ at 20, 40, and 60 m, respectively (**Table 1**).
228 These above changes are similar to those previously observed in this firn core (Li and Baker,
229 2022a), implying that the sintering-pressure mechanism plays a crucial role in the densification of
230 polar firn due to the increasing overburden of snow and firn with increasing depth. However, the
231 microstructures of the samples from the three temperatures at each depth show little variability
232 and do not monotonically change with temperature, e.g. at 20 m depth the -5°C , -18°C , and $-$
233 30°C samples having densities of $589 \pm 1.3 \text{ kg m}^{-3}$, $615 \pm 2.5 \text{ kg m}^{-3}$, and $591 \pm 1.4 \text{ kg m}^{-3}$, and

234

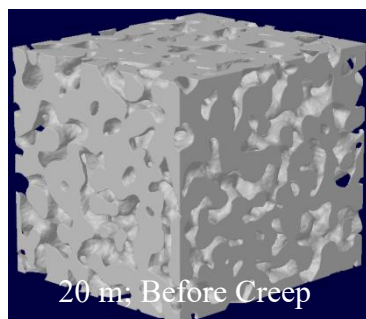
-5°C



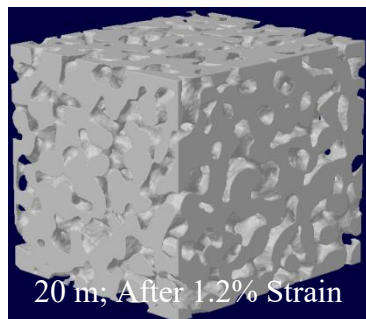
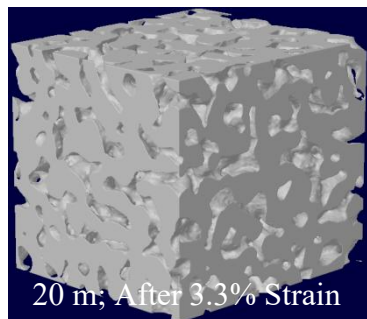
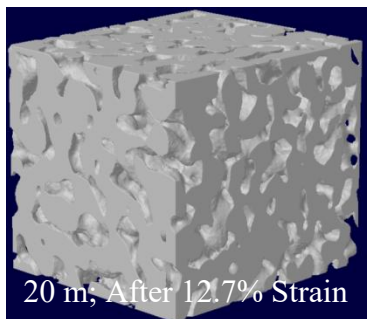
-18°C



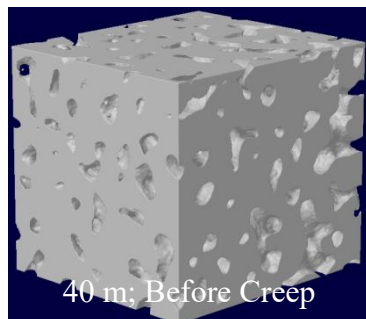
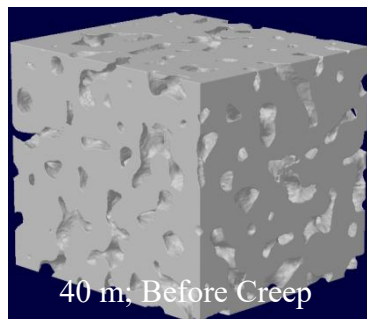
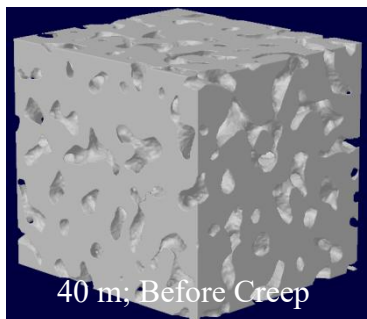
-30°C



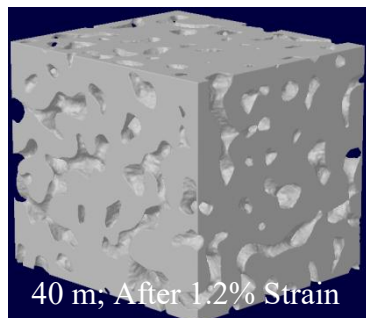
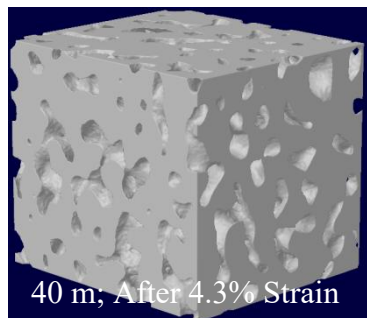
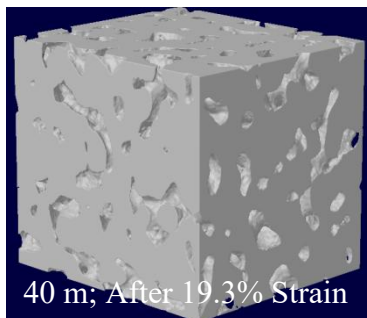
235



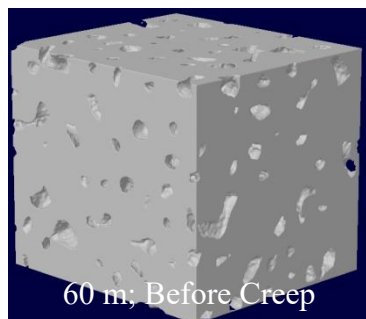
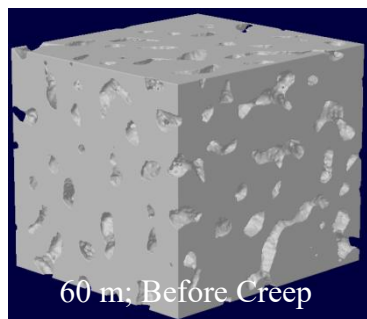
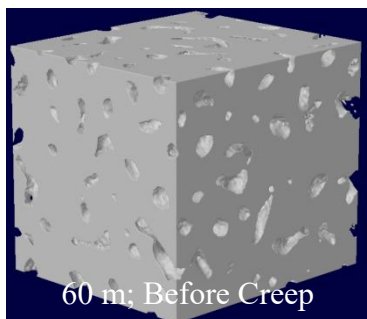
236



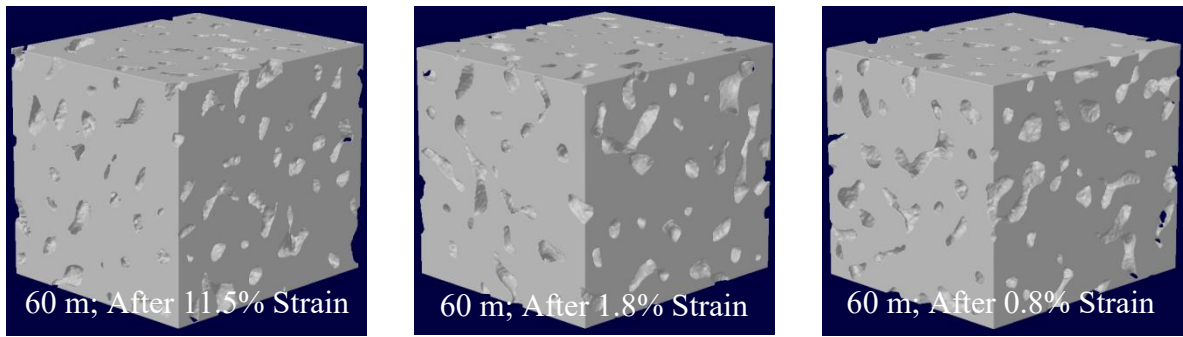
237



238



239



240

241 **Figure 2:** Micro-CT 3-D reconstructions (the side length of each cubic volume of interest is 8 mm)242 of specimens before and after creep testing at the depths and temperatures shown. Grey voxels
243 represent ice in the firn structure.

244

245

246 Table 1. Microstructural parameters derived from Micro-CT for samples at -5°C , -18°C , and -30°C from depths of 20 m, 40 m, and 60 m before creep.

20m							
T	Density	SSA	S.Th	TP	CP	SMI	ECDa
°C	kg m ⁻³	mm ⁻¹	mm	%	%		mm
-5	589±1.3	4.74±0.03	0.732±0.001	35.9±0.08	0.03±0.002	-0.31±0.04	1.07±0.005
-18	615±2.5	4.51±0.04	0.758±0.001	33.1±0.2	0.01±0.001	-0.57±0.01	0.995±0.013
-30	591±1.4	4.64±0.04	0.747±0.004	35.6±0.05	0.02±0.001	-0.27±0.05	1.09±0.004

40m							
T	Density	SSA	S.Th	TP	CP	SMI	ECDa
°C	kg m ⁻³	mm ⁻¹	mm	%	%		mm
-5	685±1.4	3.26±0.04	0.95±0.004	25.5±0.1	0.015±0.001	-1.85±0.11	0.857 ±0.005
-18	669±0.6	3.41±0.04	0.914±0.003	27.1±0.03	0.01±0.001	-1.69±0.09	0.892±0.002
-30	683±4.2	3.30±0.06	0.94±0.01	25.6±0.4	0.021±0.005	-1.87±0.13	0.86±0.01

60m							
T	Density	SSA	S.Th	TP	CP	SMI	ECDa
°C	kg m ⁻³	mm ⁻¹	mm	%	%		mm
-5	790±1.0	2.34±0.03	1.1±0.003	14.0±0.1	0.11±0.01	-4.81±0.22	0.594±0.003
-18	780±0.5	2.37±0.03	1.08±0.01	15.2±0.06	0.014±0.007	-4.8±0.2	0.632±0.001
-30	782±1.5	2.39±0.01	1.076±0.0003	14.8±0.2	0.02±0.001	-4.92±0.14	0.639±0.002

250 Note: SSA is the specific surface area, S.Th is the structure thickness, TP is the total porosity, CP

251 is the closed porosity, SMI is the structure model index, and ECDa is the area-equivalent circle
252 diameter.

253

254

255 SSAs of $4.74 \pm 0.03 \text{ mm}^{-1}$, $4.51 \pm 0.04 \text{ mm}^{-1}$, and $4.64 \pm 0.04 \text{ mm}^{-1}$, respectively (**Figures 2–3**;
256 **Table 1**). Here, despite the -18°C specimen having a higher density than the two others at -5°C
257 and -30°C , is not possible to conclude that the sintering of firn is not directly related to the
258 temperature. This is likely because a thermal equilibration period of two days in the absence of
259 compression is too short to sufficiently exert the influence of temperature on firn sintering. The
260 microstructural differences seen in these specimens more likely arose from the initial samples
261 themselves, which were anisotropic and heterogeneous even if taken from the same depth,
262 attributed to firn pre-deformation and partial annealing before experiments (Li and Baker, 2022a).

263

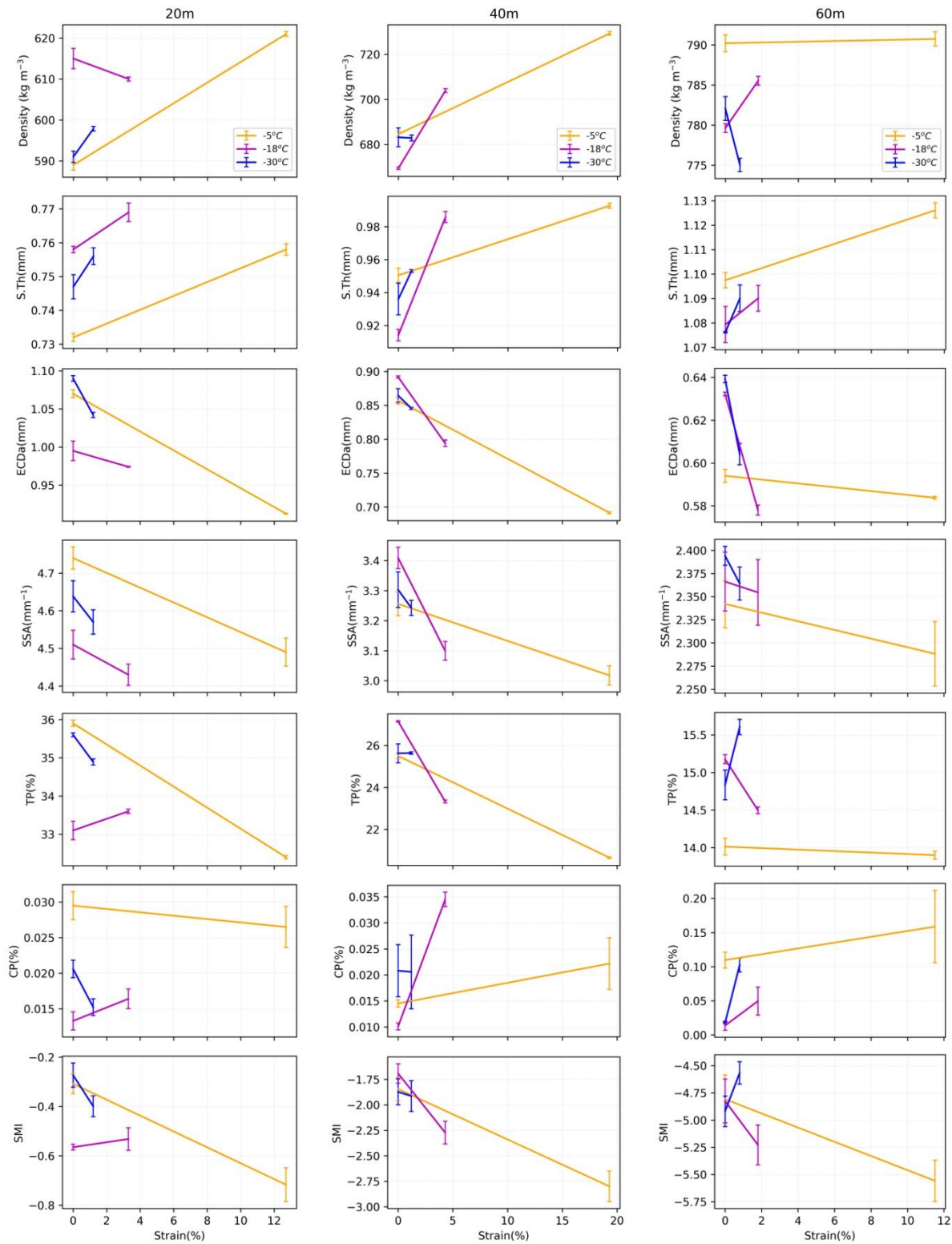
264 *3.2 Microstructures after creep*

265 The microstructural evolution is characterized by the microstructural parameters shown in **Figure**
266 **3**. The largest changes occurred in the -5°C specimens due to the higher temperature, i.e., the
267 density, S.Th, and CP increased, while the ECDa, TP, SSA, and SMI decreased, indicative of
268 consolidation of the firn after creep. It is important to note that for the 60 m sample tested at -5°C ,
269 there was no change in density, i.e., $790.2 \pm 1 \text{ kg m}^{-3}$ before creep vs. $790.7 \pm 0.9 \text{ kg m}^{-3}$ after
270 creep, or TP, i.e., $14.0 \pm 0.1\%$ before creep vs. $13.9 \pm 0.1\%$ after creep. This lack of
271 microstructural change is due to the high initial density, which was close to the firn pore close-off
272 density of $\sim 830 \text{ kg m}^{-3}$. Thus, the creep of this sample may involve a transition from firn to

273 bubbly ice, as is also indicated by the increase in CP, which would have made it difficult to
274 compress further. Intriguingly, some of the changes in microstructure observed in the micro-CT
275 3-D reconstructions from the specimens before and after creep, e.g. the distribution of ice-space,
276 are indistinguishable in **Figure 2**. This is presumably due to the relatively large initial particle size,
277 or from radial dilation exceeding the axial compression because of the small strains that occurred
278 at relatively low temperatures.

279

280 One exception to the expected microstructural change after creep was the decrease of CP, which
281 was likely due to the measurement uncertainty of the micro-CT (Burr et al., 2018), or radial
282 expansion of the specimen during creep. Another exception was the decrease in density after
283 creep for the -18°C specimen at 20 m and the -30°C specimen at 60 m, which arose due to a
284 de-densification effect produced by temperature gradient metamorphism, as confirmed by the
285 increase of both TP and S.Th (Li and Baker, 2022b). The thermal gradient appears to be
286 associated with a fluctuation of 0.2°C around the test temperature, similar to temperature cycling
287 occurred within firn (Mellor and Testa, 1969; Weertman, 1985), which stems from the
288 thermometer's inherent accuracy as noted in Section 2.2 ($-5 \pm 0.2^{\circ}\text{C}$, $-18 \pm 0.2^{\circ}\text{C}$ and $-30 \pm$
289 0.2°C). In the relatively simple deformation found at ice-sheet dome sites, such as Summit, there
290 is no mechanism to decrease density during compression. At sites closer to the ice sheet margins,
291 cracking due to extension of the ice may cause a localized decrease in density. The rate of firn
292 densification should decrease with increasing depth at a given temperature, due to the decrease of
293 effective stress with increasing depth (**Appendix A**). As a matter of fact, the density of the -5°C
294 samples after creep increased by 32 kg m^{-3} , 44 kg m^{-3} , and 0.5 kg m^{-3} for the 20 m, 40



297 **Figure 3:** Density, structure thickness (S.Th), area-equivalent circle diameter (ECDa), specific
 298 surface area (SSA), total porosity (TP), closed porosity (CP), and structure model index (SMI) of

299 the firn samples before and after creep at three temperatures (orange, magenta, and blue lines)
300 from depths of 20 m, 40 m and 60 m. Error bars indicate the variation of each microstructural
301 parameter as derived from three different VOIs of the same sample.

302

303

304 m, and 60 m samples, respectively. The 44 kg m^{-3} unexpectedly outnumbers the 32 kg m^{-3} ,
305 implying that the densification of firn is also affected by other undetermined factors, e.g. the
306 effect of inclusions, in addition to the stress and temperature.

307

308 Another way to investigate microstructure changes before and after creep tests is to compare their
309 grain sizes using thin sections. As an example, **Figure 4** shows optical micrographs of thin
310 sections made from the -5°C sample at 40 m before and after creep to a strain of 19.3%, where
311 the significant reduction in grain size from $0.8 \pm 0.67 \text{ mm}$ to $0.5 \pm 0.32 \text{ mm}$ implies the
312 occurrence of recrystallization during testing. However, it is also unclear at what strain
313 recrystallization

314

315

316

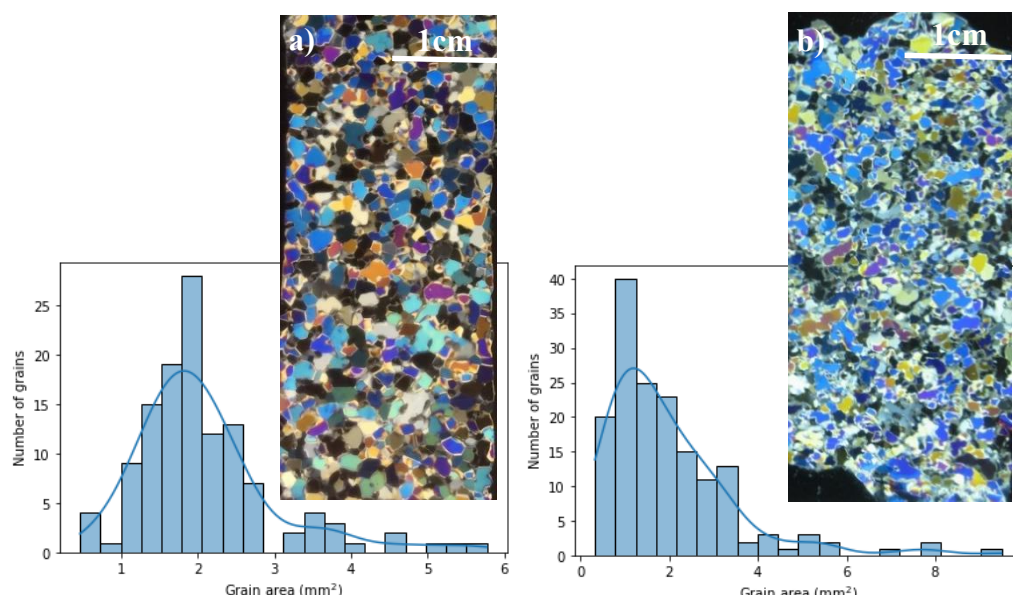
317

318

319

320

321



322

323 **Figure 4:** Optical micrographs of thin sections, and the distribution of grain sizes for the 40 m sample
324 at -5°C (a) before and (b) after creep (19.3% strain).

325

326

327 was initiated in each test, as noted in Li and Baker (2022a). Recrystallization occurs frequently at
328 a temperature higher than the homologous temperatures of $0.9 T_m$. However, no evidence was
329 found for recrystallization after testing at the relatively cold -18°C and -30°C conditions,
330 probably due to the small creep strains at these relatively low temperatures. The creep
331 mechanisms for these samples, and whether the mechanisms were different at different
332 temperatures, could not be determined from the micro-CT-derived microstructural observations
333 alone, because the micro-CT can only capture the microstructure before and after creep. Instead,
334 plots of both strain vs. time and strain rate vs. strain can be used to elucidate the onset of
335 recrystallization during creep (Sections 3.3 and 3.4; Ogunmolasuyi, et al., 2023).

336

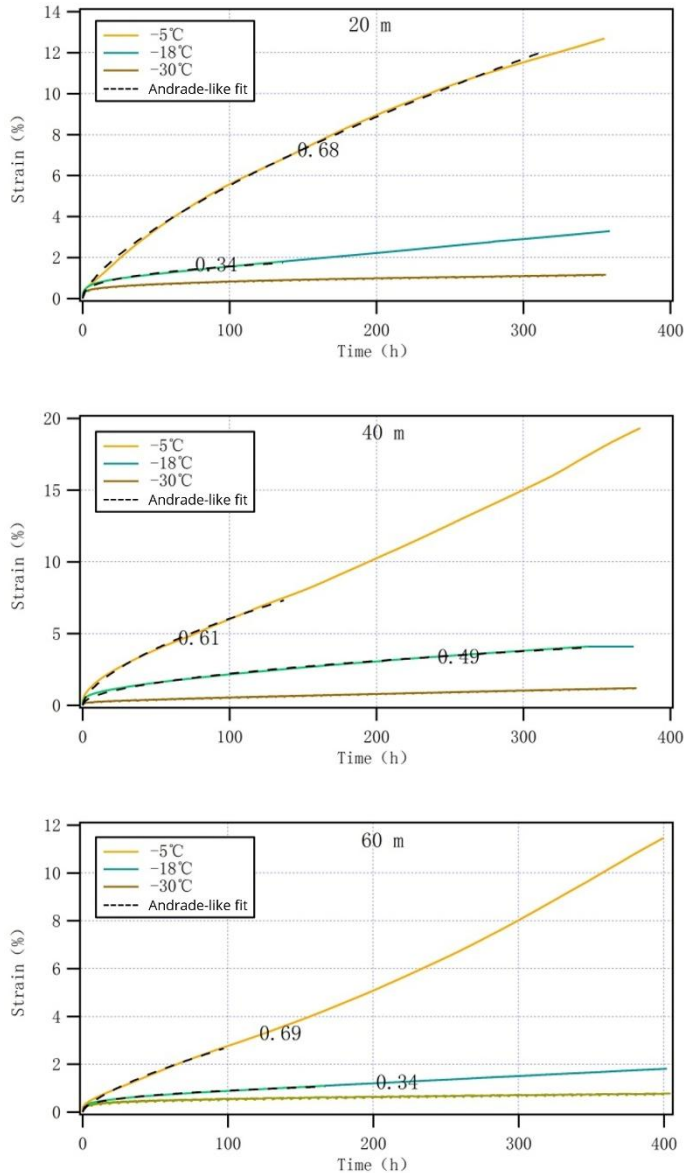
337 *3.3 Relationship between strain and time*

338 **Figure 5** shows the strain vs. time creep curves. The specimens at -5°C at 20 m and -18°C at 20
339 m, 40 m, and 60 m, show decelerating transient creep and quasi-viscous steady-state creep, while
340 the specimens at -5°C at 40 m and 60 m show transient, secondary, and accelerating tertiary creep.
341 Note that the curves from the -30°C specimens are not easily interpreted due to a large amount of
342 noise arising from both the insufficient resolution of a linear voltage differential transducer (Li
343 and Baker, 2022a) and the very small strains. The transient creep stage may be caused by strain

344 hardening that occurs from the yield point to the ultimate strength (Glen, 1955; Jacka, 1984). The
345 plastic deformation is accommodated by an increase in dislocation density through dislocation
346 multiplication or the formation of new dislocations (Frost and Ashby, 1982; Duval et al., 1983;
347 Ashby and Duval, 1985), which leads to an increase of the firn strength as the dislocations
348 become pinned or tangled, and thus more difficult to move. The initial decrease of creep rate may
349 also be related to the rearrangement of dislocations into a more stable pattern through a dragging
350 mechanism (Weertman, 1983) for the -5°C specimens. The tertiary creep stage may be associated
351 with strain softening deriving either from the thermally-activated processes at the high
352 homologous temperature approaching the melting point of ice, or from recrystallization (Li and
353 Baker, 2022a). Clearly, the creep rate of firn is sensitive to temperature under constant stress at a
354 given depth, *viz.*, the creep rate increases with increasing temperature (**Figure 5**). Incidentally,
355 there is no evidence of the onset of recrystallization in the creep curves themselves despite the
356 thin-section observation that -5°C specimens clearly underwent recrystallization during creep
357 (Section 3.2).

358

359 A modified Andrade-like equation $\varepsilon = \beta t^k + \varepsilon_0$ in Li and Baker (2022a) was used to describe the
360 transient creep behavior of the firn, in which the primary creep was well represented in black
361 dashed lines on the creep curves in **Figure 5**. The time exponent k , derived from the above
362 equation, ranges from 0.34–0.69: the data for the -30°C specimens are excluded since the noise in
363 the results makes them uninterpretable. These k values are also smaller than those from
364 monocrystalline and bicrystalline ice: 1.9 ± 0.5 , 1.5 ± 0.2 , and 1.3 ± 0.4 (Li and Baker, 2022a and
365 references therein). We also note that the k values from the specimens at -5°C from 20–60 m



366

367 **Figure 5:** Strain vs. time for firn specimens at -5°C (yellow lines), -18°C (blue lines), and -30°C (brown lines), from depths of 20 m (applied stress 0.21 MPa), 40 m (0.32 MPa) and 60 m (0.43 MPa). The black dashed curves represent fits to a modified Andrade-like equation with the time exponents indicated on the curves, if any. Note: The y-axis limits vary across the subfigures.

371

372

373 (0.68, 0.61, and 0.69), and at -18°C from 40 m (0.49) are greater than 0.33, while the k value 374 from the -18°C specimens at 20 m (0.34) and 60 m (0.34) are close to 0.33 that is usually

375 obtained for full-density polycrystal ice. Interestingly, an evident relationship between the density
376 of firn and the k values, regardless of the effect of stress (Li and Baker, 2022a) and temperature,
377 remains unknown. A greater k value signifies faster deformation. The k values derived for firn are
378 generally higher than those for polycrystalline ice, implying that the higher firn deformation rates
379 compared to those of ice ($k = \sim 0.33$; Cuffey and Paterson, 2010, and references therein) are likely
380 related to the fewer grain-boundary constraints with more void space in firn (Li and Baker, 2022a;
381 Li, 2023b). Clearly, the above k values, which increased with increasing temperature (**Figure 5**),
382 indicate that deformation is easier because of the lower viscosity at the higher temperature. Thus,
383 k seems to be a state variable with respect to temperature. In addition, k values greater than 0.33
384 may be related to the decrease of viscosity of the firn specimens (Freitag et al., 2002; Fujita et al.,
385 2014). k values lower than 0.33 observed under constant load and temperature occurred at
386 relatively low effective stresses (Li and Baker, 2022a). The identified trend of steadily declining k
387 values across the temperature range of -5°C to -18°C , however, represents a significant gap in
388 our current understanding, necessitating a dedicated investigation into the microstructural or
389 metamorphic causes. Alternatively, the enhanced cohesion strength in the firn, which resulted
390 from both the ice matrix with higher purity and the stronger bond connection of inter-grains,
391 increases the viscosity of test samples and lowers the k value to less than 0.33.

392

393 3.4 Relationship of strain rate to strain

394 **Figure 6** shows log strain rate vs. strain plots from all the -5°C and -18°C specimens; the -30°C
395 samples are excluded due to noise. The evolution of the strain rate is characterized more clearly in
396 **Figure 6** than in **Figure 5**. Clearly, the strain rate is also a state variable of temperature, where the

397 strain rate increases with increasing temperature for a given strain at a given depth (**Figure 6**;

398 **Table 2**). The strain rate minimum at the secondary creep stage (SRmin) and the strain at the

399

400

401 Table 2. Observed and inferred strain rate minima and strains observed at the strain rate minima.

20 m	SRmin s ⁻¹	PC1-SRmin s ⁻¹	PC2-SRmin s ⁻¹	PC3-SRmin s ⁻¹	Strain %
-5°C	5.53×10^{-6}	5.53×10^{-6}	1.68×10^{-6}	2.56×10^{-7}	11.8
-18°C	1.36×10^{-6}	1.36×10^{-6}	2.29×10^{-7}	2.45×10^{-8}	1.81–2.9
-30°C(U)	–	7.14×10^{-7}	2.17×10^{-7}	3.3×10^{-8}	–
-30°C(L)	–	3.16×10^{-8}	9.6×10^{-9}	1.46×10^{-9}	–

402

40 m	SRmin s ⁻¹	PC1-SRmin s ⁻¹	PC2-SRmin s ⁻¹	PC3-SRmin s ⁻¹	Strain %
-5°C	1.03×10^{-5}	3.39×10^{-5}	1.03×10^{-5}	1.57×10^{-6}	7.5
-18°C	1.4×10^{-6}	8.32×10^{-6}	1.40×10^{-6}	1.5×10^{-7}	4.1
-30°C(U)	–	4.37×10^{-6}	1.33×10^{-6}	2.03×10^{-7}	–
-30°C(L)	–	1.94×10^{-7}	5.88×10^{-8}	8.97×10^{-9}	–

403

60 m	SRmin s ⁻¹	PC1-SRmin s ⁻¹	PC2-SRmin s ⁻¹	PC3-SRmin s ⁻¹	Strain %
-5°C	5.59×10^{-6}	1.21×10^{-4}	3.67×10^{-5}	5.59×10^{-6}	2.7
-18°C	5.33×10^{-7}	2.96×10^{-5}	4.99×10^{-6}	5.33×10^{-7}	1.1–1.8
-30°C(U)	–	1.56×10^{-5}	4.74×10^{-6}	7.21×10^{-7}	–
-30°C(L)	–	6.91×10^{-7}	2.1×10^{-7}	3.19×10^{-8}	–

404 The SRmin without the prefix is the observed values during creep, while the SRmin with a prefix

405 is the inferred values. Note that PC-SRmin is the abbreviation of the post-calibration SRmin, and

406 that -30°C(U) and -30°C(L) indicate the upper and lower bound from the -30°C samples from

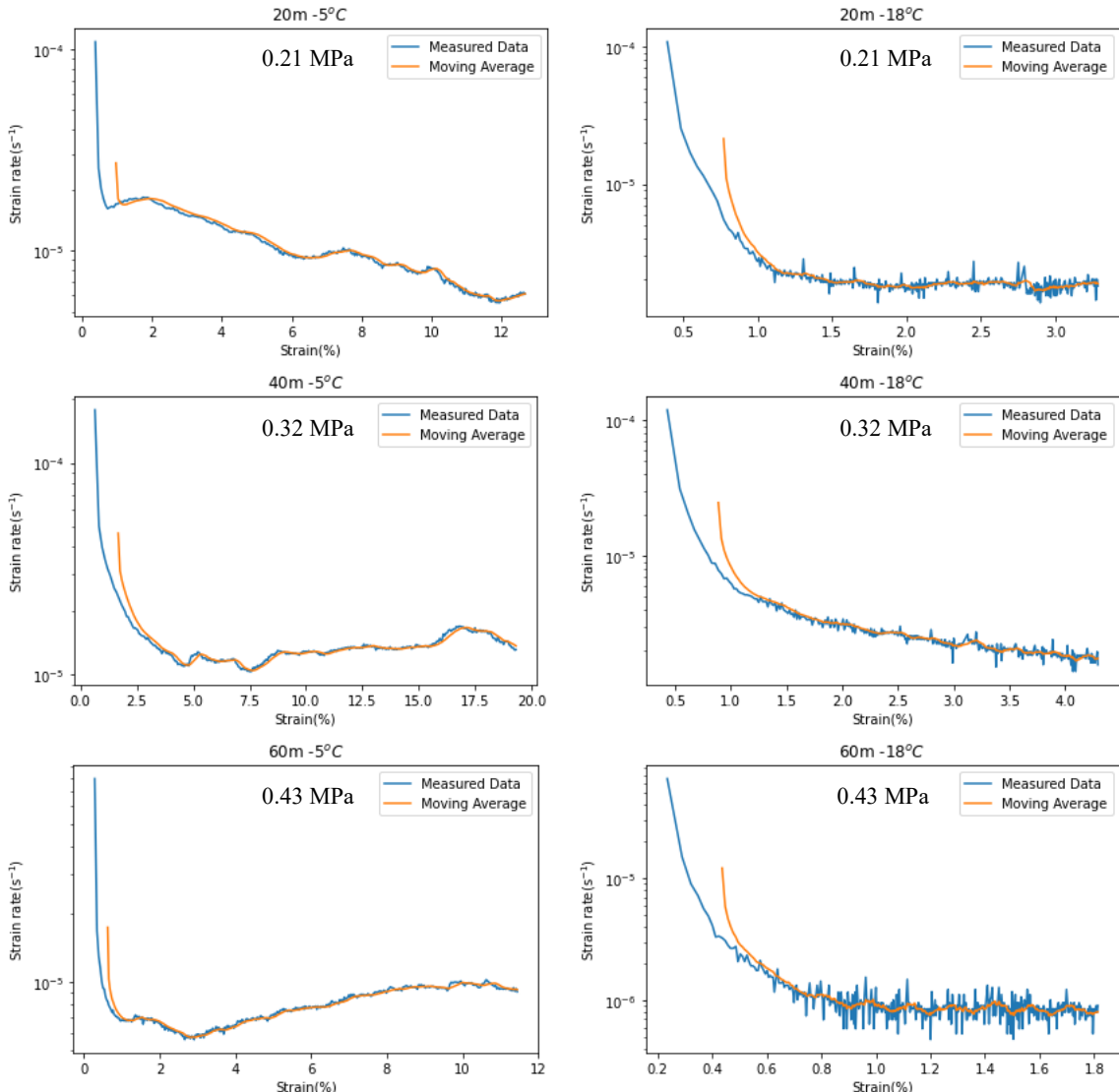
407 44.8 kJ mol⁻¹ and 113 kJ mol⁻¹, respectively. PC1-SRmin, PC2-SRmin, and PC3-SRmin are

408 described in **Appendix B**. The symbol – indicates the unavailable values of SRmin and the strain

409 value at the SRmin observed during creep. For the italics highlighted, see **Appendix B**.

410

411



412

413

414

415 **Figure 6:** Log strain rate vs. strain from the firn specimens at temperatures of -5°C and -18°C
 416 from depths of 20 m (applied stress 0.21 MPa), 40 m (0.32 MPa) and 60 m (0.43 MPa). Samples
 417 from -30°C are not shown due to the very large noise. The blue lines represent discrete strain rates,
 418 which are calculated by extracting the strain data hourly, while the orange lines represent a
 419 moving average of 15 moving windows with respect to the strain.

420

421

422 SRmin for all the -5°C and -18°C specimens are shown in **Figure 6** and **Table 2**. The SRmin was
423 reached at a strain of 11.8%, 7.5% and 2.7% for the -5°C specimens from depths of 20 m, 40 m,
424 and 60 m, respectively, consistent with strains at the SRmin decreasing with increasing depth at a
425 given temperature in **Figure 8** and **Table 4** in Li and Baker (2022a). For the -18°C specimens,
426 the SRmin occurred over a range of strains from 1.81–2.9% at 20 m, at a fixed strain of 4.1% at
427 40 m, and at a strain oscillating between 1.1 and 1.8% at 60 m. These values of strain at different
428 SRmin values are different from those usually observed at strains of 0.5–3% for fully-dense ice
429 (Cuffey and Paterson, 2010, and references therein), implying different mechanical behavior
430 between firm and pure ice (Duval, 1981; Mellor and Cole, 1983; Jacka, 1984; Li et al., 1996;
431 Jacka and Li, 2000; Song et al., 2005, 2008; Cuffey and Paterson, 2010). Overall, the strain at the
432 SRmin is greater with lower density and higher temperature, e.g. 11.8% strain from the -5°C
433 specimens at 20 m, and 4.1% strain from the -18°C specimens at 40 m. This is likely due to the
434 effect of strain hardening on density and temperature (Li, 2023b). Additionally, tertiary creep is
435 observed during both quasi-steady state deformation, particularly in the -5°C specimens at depths
436 of 40 m and 60 m, and in the ascending stage, as seen in the -5°C and -18°C specimens at 20 m,
437 along with the -18°C specimen at 40 m. This mechanical behavior is facilitated by lower firm
438 density, increased effective stress, and elevated creep temperatures. For instance, in the -5°C
439 specimens at 20 m, strain softening primarily results from recrystallization (Duval, 1981; Jacka,
440 1984; Jacka and Li, 2000; Song et al., 2005; Faria et al., 2014). Also, the activation of easy slip
441 systems contributes to this process (Jonas and Muller, 1969; Duval and Montagnat, 2002; Alley et
442 al., 2005; Horhold et al., 2012; Fujita et al., 2014; Eichler et al., 2017; Vedrine et al., 2025). It is
443 noteworthy that Jacka and Li (1994) observed that steady-state tertiary ice creep, which is marked

444 by stable grain size, is influenced more by applied stresses than by temperature. This finding
445 suggests that there exists a balance between the activation energies required for grain growth and
446 subdivision at a specific temperature.

447

448 *3.5 Apparent activation energy for creep*

449 Experimental observations of the SRmin are limited, as they only occurred for the -5°C and at $-$
450 18°C specimens at each depth (**Table 2**). It is hard to achieve the SRmin for all firn specimens in
451 laboratory environments (Landauer, 1958), especially under low temperatures and stresses such as
452 those from the -30°C specimens in this work. To this end, we offer the various possibilities of the
453 SRmin using the evidence we have. The value of the apparent activation energy of creep, Q_c (kJ
454 mol^{-1}), is equal to the slope of a line fitted $\ln \dot{\varepsilon}$ versus $1/T$ as did in Goldsby & Kohlstedt (1997;
455 2001), using the Arrhenius relation $\dot{\varepsilon} = B\sigma^n \exp(-\frac{Q_c}{RT})$, where $\dot{\varepsilon}$ (s^{-1}) is the strain rate, B (s^{-1}
456 Pa^{-n}) is the material parameter, σ (MPa) is the applied stress, n is the creep (stress) exponent, R
457 ($8.314 \text{ J mol}^{-1} \text{ K}^{-1}$) is the gas constant, and T (K) is Kelvin temperature. It is noted that under
458 constant-stress conditions, the value of the stress exponent n influences the pre-exponential factor
459 B but does not affect the slope of the Arrhenius plot and therefore the derived activation energy Q_c .
460 First, the estimation of Q_c is based on *only* two SRmin values from the -5°C and -18°C samples
461 at each depth (**Table 2**). Glen-King's model $\dot{\varepsilon} = A \exp(-Q_c/RT) = B\sigma^n \exp(-Q_c/RT)$ treats the
462 pre-factor A , material parameter B , and stress exponent n as constants (Glen, 1955; Goldsby and
463 Kohlstedt, 2001). This simplification is valid by using the unifying concept of normalized
464 effective stress. The effective stress captures the complex multi-physical behavior of the
465 two-phase ice-air system, accounting for: 1) The incompressibility of individual ice grains versus

466 the compressibility of the porous ice skeleton, 2) The coupled flow of ice and air; and 3) The
 467 interplay between different strain components (axial, radial, volumetric, and true). This
 468 framework is grounded in the principles of poromechanics, originally developed for soils and
 469 later applied to snow and ice (Gubler, 1978; Hansen and Brown, 1988; Mahajan and Brown, 1993;
 470 Chen and Chen, 1997; Lade and deBoer, 1997; Ehlers, 2002; Khalili et al., 2004; Gray and
 471 Schrefler, 2007; daSilva et al., 2008; Nuth and Laloui, 2008). The variability in density for the
 472 samples from 20-m depth on the mechanical behavior are negligible due to a small difference (up
 473 to ~4%), between samples, which falls within an acceptable error range in previous studies. This
 474 is likely related to multiple factors, including the intrinsic properties of the samples, e.g.
 475 inclusions (impurities, dust, bubbles, clathrate hydrates), the effects of deformation and partial
 476 annealing of firn due to stress distribution and temperature changes during drilling, extraction,
 477 transportation, or storage, and the fact that the samples are taken from adjacent parts of the core,
 478 and might capture heterogeneous density layers, as well as potential measurement errors
 479 associated with the equipment used. The Q_c values from the 20 m, 40 m, and 60 m specimens
 480 were calculated to be 61.4 kJ mol^{-1} , 87.3 kJ mol^{-1} , and 102.8 kJ mol^{-1} , respectively (**Figure 7**).
 481 Based on the three SRmin from the -5°C and -18°C samples at 60 m in this work, and from $-$
 482 10°C samples at 60 m in Li and Baker (2022a), a Q_c value for the 60 m specimen was calculated
 483 to be 100.7 kJ mol^{-1} . To see whether or not these above Q_c values are reliable, we estimated the
 484 activation energy of grain-boundary diffusion/viscosity, Q_{gbd} (kJ mol^{-1}), using the relation
 485
$$K = (D_t^2 - D_0^2)/t = k \exp(-Q_{\text{gbd}}/RT)$$
, in an alternative form of $Q_{\text{gbd}} = -R[\partial \ln K / \partial (1/T)]$,
 486 where K is the observed rate of grain growth ($\text{mm}^2 \text{a}^{-1}$), D_0^2 and D_t^2 are the measured mean
 487 grain area (mm^2) in a firn sample at the onset of the creep ($t = 0$), and at the end time of the creep

488 (t -year), and k is a constant grain growth factor. The grain growth rates are plotted on a
489 logarithmic scale against the reciprocal of T (**Figure 7**). For changes in grain size from the related
490 specimens before and after creep see **Table 3**. Correspondingly, the Q_{gbd} values calculated were
491 41.4 kJ mol^{-1} , 40.8 kJ mol^{-1} , and 40.9 kJ mol^{-1} for the specimens at 20 m, 40 m, and 60 m,
492 respectively. These Q_{gbd} values are comparable to the values of 40.6 kJ mol^{-1} obtained in
493 laboratory experiments on polycrystalline ice (Jumawan, 1972), and 42.4 kJ mol^{-1} from 13 polar
494 firn cores (Cuffey and Paterson, 2010) for grain-boundary self-diffusion of polycrystalline ice.
495 Further, the ratio of Q_{gbd}/Q_c is 0.67, 0.47, and 0.4 for the 20 m, 40 m, and 60 m specimens,
496 respectively. We noted that the ratio of 0.67 for Q_{gbd}/Q_c was recommended by Hobbs (1974) and
497 Cuffey and Paterson (2010). The Q_c values calculated using the Arrhenius relation for the 40 m
498 and 60 m specimens are likely greater than the actual values, and hence are seemingly less
499 reliable. There is little difference between the two-SRmin-derived Q_c value ($102.8 \text{ kJ mol}^{-1}$) and
500 the three-SRmin-derived Q_c value ($100.7 \text{ kJ mol}^{-1}$), implying that these two avenues for
501 calculating Q_c have equal utility. Moreover, the above Q_{gbd} values are lower than the 48.6 kJ
502 mol^{-1} that was inferred by the grain growth rate for firn samples with densities ranging from 320–
503 650 kg m^{-3} from cores drilled at the South Pole, Antarctic (Gow, 1969), which makes a ratio of
504 0.67 for Q_{gbd}/Q_c an unreliable sole-criterion. In short, it is difficult to assess the reliability of both
505 Q_c and Q_{gbd} , as discussed above due to their scatter and debates in the current literature. Thus,
506 these Q_c values estimated in this work, ranging from $61.4\text{--}102.8 \text{ kJ mol}^{-1}$, are reasonable,
507 aligning with the literature range of $44.8\text{--}113 \text{ kJ mol}^{-1}$ (**Table 4**).

508

509

510 Table 3. Grain area (mm^2) measured from optical thin sections for samples at -5°C , -18°C , and $-$
511 30°C from depths of 20 m, 40 m, and 60 m before and after creep.

Depth	20 m		40 m		60 m	
	T/ $^\circ\text{C}$	Before	After	Before	After	Before
-5	0.29 ± 0.25	0.42 ± 0.28	0.53 ± 0.32	0.79 ± 0.67	0.78 ± 0.67	0.97 ± 0.8
-18	0.29 ± 0.25	0.34 ± 0.2	0.53 ± 0.32	0.7 ± 0.42	0.78 ± 0.67	0.9 ± 0.59
-30	0.29 ± 0.25	0.31 ± 0.17	0.53 ± 0.32	0.57 ± 0.34	0.78 ± 0.67	0.81 ± 0.56

512

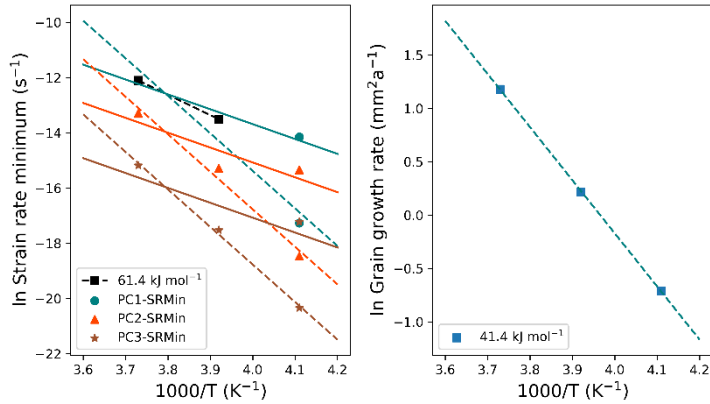
513

514 A great challenge is the estimation of the Q_c using the SRmin including the -30°C specimens,
515 whose SRmin shows high variability due to the extraordinarily slow strain rate at low
516 temperatures. This difficulty cannot be resolved by extrapolating experimental data (Sinha, 1978;
517 Hooke et al., 1980), e.g. the use of Andrade's law (Glen, 1955). Instead, we turned our focus to
518 studying the relationship between the SRmin and temperature by constraining our data in a wide
519 range of Q_c values reported in existing literature presented in **Table 4**. Clearly, there is a larger
520 scatter of Q_c values for firn than for ice. The increase of Q_c from mono-crystalline and
521 bi-crystalline to polycrystalline ice implies that the greater the reduction in the constraint from
522 grain boundaries, the greater is Q_c . Alternatively, firn creep is easier than that of polycrystalline
523 ice due to either the easier sliding of grains in firn along more directions in the more porous and
524 heterogeneous structure (Section 3.3), or the decrease of viscosity associated with inclusions (e.g.

525

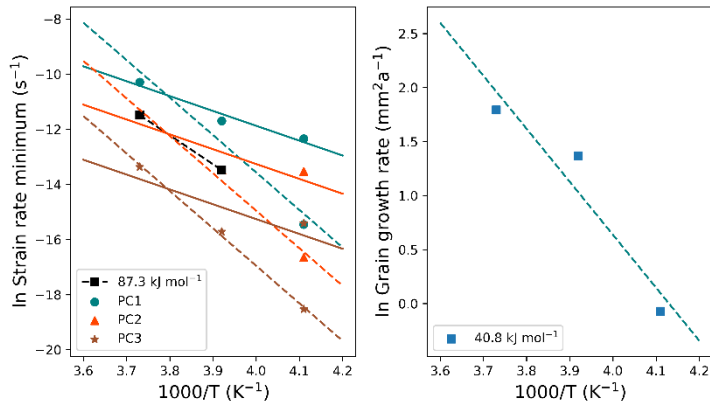
526

Activation energy for the 20 m specimens



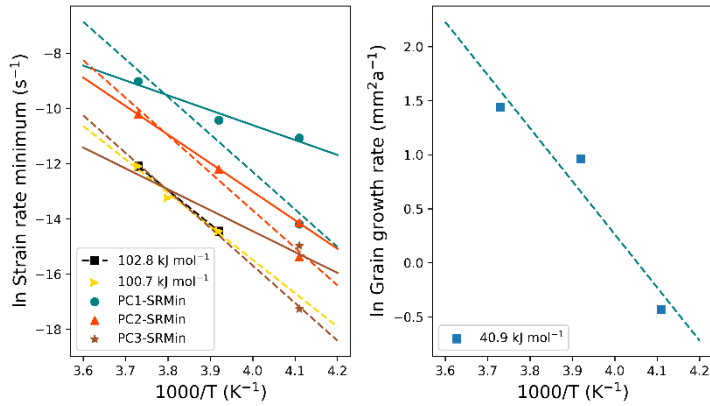
527

Activation energy for the 40 m specimens



528

Activation energy for the 60 m specimens



529

530 **Figure 7:** Arrhenius plots to estimate the apparent activation energy of creep (Q_c ; left panel) and
 531 the apparent activation energy of grain-boundary diffusion (Q_{gbd} ; right panel) from the firm
 532 specimens noted. The teal, orange, and brown solid lines are the upper bound (44.8 kJ mol⁻¹) of
 533 PC1-SRmin, PC2-SRmin, and PC3-SRmin, respectively, while the teal, orange, and brown dashed

534 lines are the lower bound (113 kJ mol⁻¹) of PC1-SRmin, PC2-SRmin, and PC3-SRmin,
 535 respectively (Table 2). The teal circles, the orange triangles, and the brown stars are the data in
 536 Table 2. The black dashed lines are from *only* two SRmins at -5°C and -18°C (the black squares
 537 are the data measured), whose Q_c is indicated in each subfigure. The yellow dashed line is from
 538 the three SRmins at -5°C, -18°C in this work, and -10 °C from Li and Baker (2022a) (the yellow
 539 triangles are the measured data), whose Q_c is 110.7 kJ mol⁻¹. The blue dashed lines (right panel)
 540 are from grain growth rate at three temperatures (the blue squares are the observed data), whose
 541 Q_{gbd} is indicated in each subfigure.

542

543

544 Table 4. Apparent activation energy for the creep of firn and ice, Q_c , reported in literature.

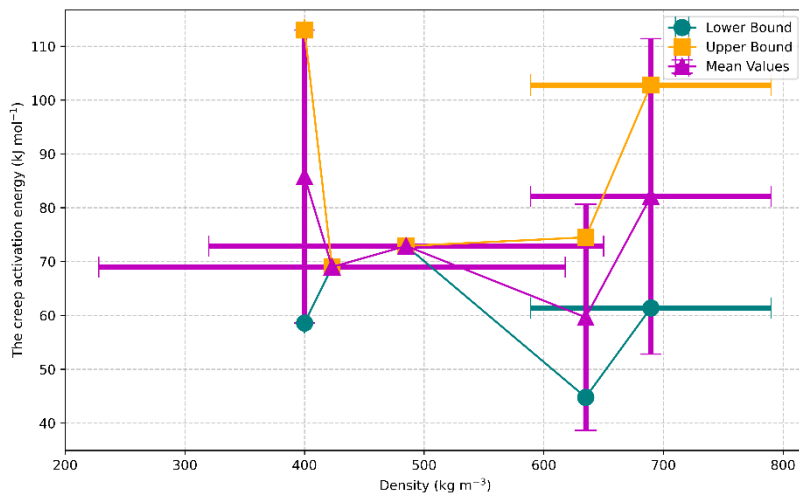
Q_c kJ mol ⁻¹	Sample	Density kg m ⁻³	Temperature °C	Methods	Source
58.6–113	Firn	~400	[-13.6, -3.6]	Uniaxial/Hydrostatic Compression	Landauer (1958)
44.8–74.5	Firn/Bubbly Ice	440–830	[-34.5, -0.5]	Uniaxial Unconfined Compression	Mellor and Smith (1966)
54	Firn/Bubbly Ice	Undetail ed	[-28, -16]	Shear Deformation of Boreholes	Paterson (1977)
~72.9	Firn	320–650	Unnecessary	Grain Growth Rate	Gow (1969)
69 ± 5	Firn	423 ± 8	[-19, -11]	Triaxial Compression	Scapozza and Bartelt (2003)
~60	Artificial/Natural Ice (South Pole)	~917	-15	Torsion Creep Test	Pimienta and Duval (1987)
61	Polycrystalline Ice	~917	-9.6	Hydrostatic Pressure	Duval et al. (1983)
78	Monocrystalline Ice	~917	[-30, -4]	Derived from Bicrystal Ice	Homer and Glen (1978)
75	Ice Bicrystal	~917	[-30, -4]	Tensile Test Parallel to Grain-boundary	Homer and Glen (1978)

545

546

547 Baker and Gerberich, 1979; Goodman et al., 1981) that facilitate the intra- and inter-grain sliding
 548 (Salamatin et al., 2009). In principle, Q_c of firn should exceed that for polycrystalline ice.
 549 Intriguingly, some reported Q_c values from firn are less than that for ice, meaning the degree of
 550 spatial freedom in the ice-matrix is limited by the topological structure of the firn (Liu et al.,
 551 2022). Incidentally, the effective stress of porous materials is determined by not only its porosity,
 552 but also other factors, e.g. the microstructural topology (Liu et al., 2022) and the impurity types
 553 and concentrations in the firn. However, this issue is beyond the scope of this work. In seeking a
 554 conclusion, we evaluated the dependence of creep activation energy on firn density. The data
 555 indicate no discernible relationship between these two parameters (Fig. 8). In summary, a Q_c for
 556 firn, which ranges from 44.8–113 kJ mol⁻¹, is plausible due to the intrinsic nature of natural firn
 557 that has a far more complicated and changeable microstructure than ice.

558



559

560 **Figure 8:** Plots of the creep activation energy vs. firn densities. For each density, three values are
 561 shown: the lower bound (minimum activation energy, teal), the upper bound (maximum activation
 562 energy, orange), and the mean value (magenta). Error bars represent the standard deviation of the

563 mean. Data are sourced from Table 4 and the present study.

564

565

566 The value of the stress exponent n is determined by plotting the line fit the logarithm relation of
567 the steady-state strain rate, $\dot{\varepsilon}$, versus the effective stress, σ , and is, thus, the slope of this line
568 from the measured SRmins (**Table 2**). We determined stress exponent (n) values of approximately
569 0.1 and -1.2 for the -5°C and -18°C samples based on observed data, respectively. This result
570 directly contradicts the value of $n \approx 4.3$ reported from the same Greenland firn core by Li and
571 Baker (2022a). Further, these values fall entirely outside the established range of ~ 1 to ~ 7.5
572 (mean $\sim 4.25 \pm 3.25$) documented across decades of ice mechanics literature (Glen, 1955; Hansen
573 and Landauer, 1958; Butkovich and Landauer 1960; Kamb, 1961; Paterson and Savage, 1963;
574 Higashi et al, 1965; Mellor and Testa, 1969; Raymond, 1973; Hooke, 1981; Thomas et al., 1980;
575 Duval et al., 1983; Weertman, 1983,1985; Azuma and Higashi, 1984; Pimienta and Duval, 1987;
576 Budd and Jacka, 1989; Jacka and Li, 1994; Goldsby and Kohlstedt, 2001; Bindschadler et al.,
577 2003; Cuffey, 2006; Chandler et al. 2008; Cuffey and Kavanaugh, 2011; McCarthy et al., 2017;
578 Millstein et al., 2022; Colgan et al., 2023; Li, 2025). The wide range of reported n -values is
579 governed by a complex interplay of deformation mechanisms—including grain boundary sliding,
580 diffusion (lattice and grain boundary), and dislocation processes, e.g. hard-slip-dominated,
581 dislocation-accommodated grain boundary sliding, and grain boundary sliding-limited basal
582 dislocation—across varying stresses, temperatures, crystallographic fabrics, impurity contents, and
583 grain-size-to-sample-size ratios. We attribute the significant discrepancy in these findings to the
584 experimental conditions. The lower temperatures used (down to -30°C) induce slower strain rates,

585 which prevented the tests from reaching a critical strain rate minimum (SRMin). Therefore, to
586 accurately estimate the activation energy for deformation, it is necessary first to calibrate the
587 SRMin value for all noised samples. A constant stress exponent value of $n \approx 4.3$ (Li and Baker,
588 2022a) was used to compute the activation energy. This necessary simplification—an
589 acknowledgement of current methodological limitations rather than a dismissal of the underlying
590 physics—introduces a key uncertainty that highlights the need for future advancements in
591 observational methodology within firn research. To proceed, the post-calibration SRmins for the –
592 5°C and –18°C samples are highlighted in **Table 2** (see **Appendix B** in detail). It is important to
593 note that the stress exponent does not depend on the density of the tested samples, thereby
594 negating any basis for discussing a relationship between the stress exponent and sample density.
595 Instead, variations in stress corresponding to density variations are manifested in the strain rate,
596 ensuring that the derivation of the stress exponent and activation energy remains consistent. From
597 here on we only discuss the applied stress since there is little difference between the effective
598 stress and applied stress for calculating the stress exponent (Li and Baker, 2022a). Based on both
599 the reported range of Q_c and the two observed SRmins at –5°C and –18°C, the SRmins for the
600 –30°C samples are inferred (**Table 2**), using the Arrhenius relation. Also, based on both the
601 observed and inferred SRmins with the upper and lower bounds (**Table 2**), a series of fitted
602 functions are then found between the SRmin and the reciprocal of the temperature (°C), $1/T_c$:
603
604 20-m samples:

605

$$\left\{ \begin{array}{l} \text{SRMin} = -3 \times 10^{-5} / T_c - 7 \times 10^{-7} [R^2 = 0.988; \text{PC1(L 20)}] \\ \text{SRMin} = -3 \times 10^{-5} / T_c - 2 \times 10^{-7} [R^2 = 1; \text{PC1(U 20)}] \\ \text{SRMin} = -1 \times 10^{-5} / T_c - 3 \times 10^{-7} [R^2 = 1; \text{PC 2(L 20)}] \\ \text{SRMin} = -9 \times 10^{-6} / T_c - 2 \times 10^{-7} [R^2 = 0.987; \text{PC 2(U 20)}] \\ \text{SRMin} = -2 \times 10^{-6} / T_c - 6 \times 10^{-8} [R^2 = 0.998; \text{PC 3(L 20)}] \\ \text{SRMin} = -1 \times 10^{-6} / T_c - 3 \times 10^{-8} [R^2 = 0.976; \text{PC 3(U 20)}] \end{array} \right. ,$$

606 40-m samples:

607

$$\left\{ \begin{array}{l} \text{SRMin} = -2 \times 10^{-4} / T_c - 4 \times 10^{-6} [R^2 = 0.988; \text{PC1(L 40)}] \\ \text{SRMin} = -2 \times 10^{-4} / T_c - 2 \times 10^{-6} [R^2 = 1; \text{PC1(U 40)}] \\ \text{SRMin} = -6 \times 10^{-5} / T_c - 2 \times 10^{-6} [R^2 = 1; \text{PC2(L 40)}] \\ \text{SRMin} = -6 \times 10^{-5} / T_c - 1 \times 10^{-6} [R^2 = 0.987; \text{PC2(U 40)}] \\ \text{SRMin} = -1 \times 10^{-5} / T_c - 3 \times 10^{-7} [R^2 = 0.998; \text{PC3(L 40)}] \\ \text{SRMin} = -9 \times 10^{-6} / T_c - 2 \times 10^{-7} [R^2 = 0.976; \text{PC3(U 40)}] \end{array} \right. ,$$

608 60-m samples:

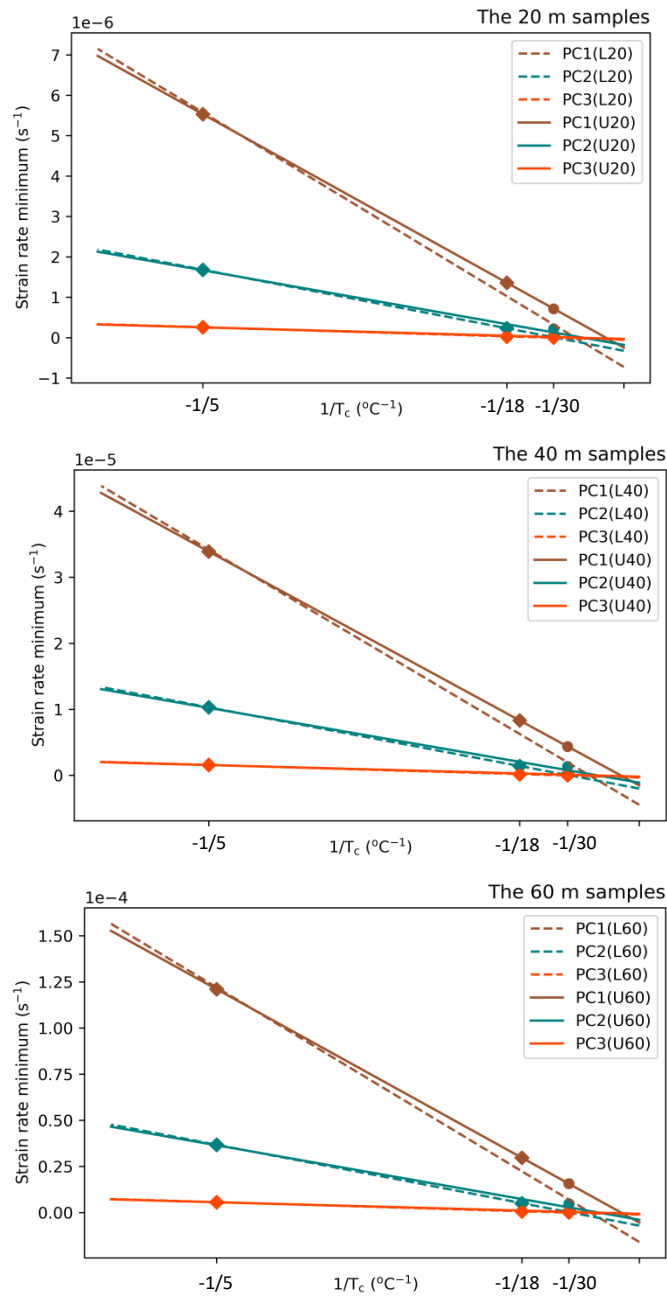
609

$$\left\{ \begin{array}{l} \text{SRMin} = -7 \times 10^{-4} / T_c - 2 \times 10^{-5} [R^2 = 0.988; \text{PC1(L 60)}] \\ \text{SRMin} = -6 \times 10^{-4} / T_c - 6 \times 10^{-6} [R^2 = 1; \text{PC1(U 60)}] \\ \text{SRMin} = -2 \times 10^{-4} / T_c - 7 \times 10^{-6} [R^2 = 1; \text{PC2(L 60)}] \\ \text{SRMin} = -2 \times 10^{-4} / T_c - 4 \times 10^{-6} [R^2 = 0.987; \text{PC2(U 60)}] \\ \text{SRMin} = -3 \times 10^{-5} / T_c - 1 \times 10^{-6} [R^2 = 0.998; \text{PC3(L 60)}] \\ \text{SRMin} = -3 \times 10^{-5} / T_c - 7 \times 10^{-7} [R^2 = 0.976; \text{PC3(U 60)}] \end{array} \right. ,$$

610

611 where PC1(L20) and PC1(U20) indicate the lower and upper bound values of the post-calibration
 612 SRmins from the 20 m samples (**Table 1**), and other symbols are similarly formatted, e.g.
 613 PC1(L40), PC1(U40), PC1(L60), PC1(U60), and so on. These relationships are plotted in **Figure**
 614 **8**, where the SRmin vs. $1/T_c$ plots from the three depths are almost the same shape, implying that
 615 the SRmin is dependent on the temperature at a constant stress. It is important to note that the
 616 average (minimum) strain rate for the secondary creep stage for a given temperature increases
 617 with increasing depth/density of the samples (**Figure 8; Table 2**). This is opposite to a decrease of

618 the SRmin at a fixed stress and temperature in **Figure 8** and **Table 4** in Li and Baker (2022a).
619 These changes in SRmin are irrespective of the stress (**Appendix A**). The temperature plays a
620 predominant role during firn creep for a given density of sample at a constant stress. An
621 interesting question on firn creep at a specific temperature is whether the SRmin slows down or
622 speeds up with decreasing density of firn. Certainly, natural firn samples raise the complexity in
623 interpreting the firn creep due to the influences both from inclusions (Li and Baker, 2022a and
624 references therein; Li, 2024), and from the topology of the microstructures (Liu et al., 2022). In
625 addition, there is a broad spread of the SRmin at each depth, in which the SRmin varies by several
626 times, even one order of magnitude or more between the different possibilities of post-calibration
627 SRmins (**Figure 8**), implying that the microstructure of the sample significantly influences the



644 **Figure 9:** Plots of the strain rate minimum versus the reciprocal of temperature. PC1(L20) and
 645 PC1(U20) indicates the lower and upper bound, respectively, from the 20 m samples via PC1 as
 646 noted in Table 2, and so on. The circles indicate the upper bound data measured and inferred,
 647 while the squares indicate the lower bound data. The dashed line is the fit from the lower bound,
 648 while the solid line is the fit from the upper bound.

649

650

651 process of the creep of firn. Moreover, it is hard to generalize a universal formula for predicting
652 the SRmin at temperatures below -30°C , where the SRmins becomes negative (**Figure 8**). Thus,
653 there is a need for an in-depth understanding of the polar firn creep behavior in secondary creep
654 stage.

655

656 To illustrate the differences between the Q_c values calculated from PC1-SRmin, PC2-SRmin,
657 and PC3-SRmin, we have plotted them in **Figure 7**. Interestingly, the Arrhenius plots of the
658 natural logarithm of strain rate with $1000/T$ (**Figure 7**) are similar to those observed by Glen
659 (1955) and Homer and Glen (1978), implying that there is no significant difference in the creep
660 mechanism for a temperature range of -30°C to -5°C (Glen, 1955; Homer and Glen, 1978),
661 where both diffusion via grain-boundary, vacancy or interstitial defects (Barnes et al., 1971;
662 Brown and George, 1996; Nasello et al., 2005; Li and Baker, 2022b), and dislocations contribute
663 to the creep of polar firn.

664

665 **4. Conclusions**

666 Constant-load creep tests were performed on three cylindrical specimens tested from depths of 20
667 m (applied stress 0.21 MPa), 40 m (0.32 MPa) and 60 m (0.43 MPa) at temperatures of $-5 \pm$
668 0.2°C , $-18 \pm 0.2^{\circ}\text{C}$, and $-30 \pm 0.2^{\circ}\text{C}$ from a firn core extracted at Summit, Greenland in June
669 2017. The microstructures were characterized before and after creep testing using the micro-CT
670 and thin sections viewed between optical crossed polarizers. It was found that:

671

672 1. Microstructural parameters measured using the micro-CT show that the polar firn densified
673 during the creep compression (e.g. from 685 to 729 kg m⁻³ for the 40 m specimen at -5°C),
674 *viz.*, the TP (from 25.5 to 20.7%), the ECDA (from 0.86 to 0.69 mm), the SSA (from 3.26 to
675 3.02 mm⁻¹), and the SMI (from -1.85 to -2.8) decreased, while the S.Th (from 0.95 to 0.99
676 mm) and the CP (from 0.01 to 0.02%) increased. Anomalies in the microstructures, especially
677 at low temperatures of -18°C and -30°C, are likely due to metamorphism under temperature
678 gradients, the radial dilation effect during firn deformation, the measurement uncertainty of
679 the micro-CT, or the anisotropy and the heterogeneity of natural firn.

680 2. The transient creep behavior of firn at constant stress and different temperatures obeys an
681 Andrade-like law, but, the time exponent k of 0.34–0.69 is greater than the 0.33 found for ice.
682 This is due to fewer grain-boundary constraints in porous firn than in ice.

683 3. The secondary creep behavior of firn at constant stress and different temperatures presented
684 here shows that the strain at the SRmin increases with decreasing firn density and increasing
685 creep temperature. In particular, low-density firn during creep at high temperatures shows that
686 the strain at the SRmin, e.g. 11.8% and 7.5% respectively from the 20 m and 40 m specimens
687 at -5°C, is greater than the strain of 3%, which is the maximum found at the SRMin of ice.

688 4. The tertiary creep behavior of firn at constant stress and different temperatures is more easily
689 observed from lower-density specimens at greater effective stresses and higher creep
690 temperatures. The strain softening in tertiary creep is primarily due to recrystallization.

691 5. The apparent activation energy for the firn creep has a wide range of 61.4–102.8 kJ mol⁻¹
692 because the grains in firn slide more easily along more directions in the more porous and
693 heterogeneous structure, the enhanced fluidity from inclusions, and the topological structure

694 of the firn. In addition, the SRmin is a function of the temperature, depending on the
695 microstructure of firn and the inclusion content. The predicted SRmin increases with
696 increasing firn density at a given temperature and is independent of the effective stress. Lastly,
697 there is no significant difference in the creep mechanism at temperatures ranging from -30°C
698 to -5°C .

699

700 The creep of polar firn behaves differently from full-density ice, implying that firn densification is
701 an indispensable process in fully understanding the transformation of snowfall to ice in the polar
702 regions. Observed firn deformation indicates that temperature plays a determined role in firn
703 densification. Thereby, it will be helpful to bridge a gap between the firn temperature and the
704 climate of the past for reconstructing paleoclimate. Also, it will be helpful to apply a confining
705 load to investigate the microstructure of the creep of polar firn with smaller initial particle sizes at
706 low temperatures using the micro-CT. Further studies of interest are to investigate the quantitative
707 relationship between the microstructural parameters and the mechanical behavior of polar firn,
708 and when the onset of recrystallization occurs during creep, as well as verify the SRmin predicted
709 by the relationship of SRmin vs. temperature from the firn specimens at more extensive ranges of
710 stresses and temperatures.

711 **Appendix A: Hydrostatic pressure, the applied stress, and the effective stress**

712 The hydrostatic pressure, p , which varies with temperature, along with the cohesion of the ice and
713 the friction angle between snow particles, plays a significant role in determining the apparent
714 activation energy and, consequently, the strength of the ice (Fish, 1991). It was calculated from
715 the overburden pressure of snow, i.e. $p = \bar{\rho}_f gh$, where $\bar{\rho}_f$ is the average firm density above the
716 depth of interest, h , and g is the acceleration of gravity. At Summit, p at the depths of 20 m, 40 m,
717 and 60 m was estimated to be ~ 0.1 MPa, ~ 0.22 MPa, and ~ 0.38 MPa, respectively. Note that the
718 slope of the surface of ice sheets and glaciers at Summit is idealized to be zero, i.e., their surfaces
719 are horizontal. The applied stress, σ , is the applied load divided by the cross-sectional area of a
720 sample. The σ at the depths of 20 m, 40 m, and 60 m were 0.21 MPa, 0.32 MPa, and 0.43 MPa,
721 respectively. The effective stress, $\tilde{\sigma}$, is defined as σ divided by the fraction of ice matrix in
722 firn, see in detail from Li and Baker (2022a). Thereby, $\tilde{\sigma}$ is 0.32 MPa (the mean porosity of
723 34.9%), 0.43 MPa (24.8%), and 0.5 MPa (14.4%) from the 20–60 m samples, respectively. Note
724 that the stresses were vertically loaded on the sample (parallel to the direction of core axis of the
725 sample) in laboratory tests. Ideally, in order to be analogous to the densification of firn in nature,
726 $\tilde{\sigma}$ for laboratory samples from a given depth should be equal to the p of firn *in situ* at an
727 equivalently same depth at Summit, namely $\tilde{\sigma}/p = 1$. However, in consideration of the laboratory
728 timeframe for experiments (Pimienta and Duval, 1987), the stresses applied in laboratory tests are
729 usually higher with a resulting higher rate of deformation than those *in situ*. Thus, to observe the
730 effect of the stress on the creep of firn with different densities at different depths, we designed the
731 following configuration of the $\tilde{\sigma}/p$ with depth, *viz.*, $0.32 \text{ MPa}/\sim 0.1 \text{ MPa} = \sim 3.2$, $0.43 \text{ MPa}/\sim 0.22$
732 MPa = ~ 1.95 , and $0.5 \text{ MPa}/\sim 0.38 \text{ MPa} = \sim 1.32$ for the samples from the depths of 20 m, 40 m,

733 and 60 m, respectively. In this manner, the decrement of $\tilde{\sigma}/p$ with increasing depth represents
734 the decrease of the effective stress with increasing depth. Also, it's important to note that the
735 strain rates achieved during creep experiments in laboratory settings are 6 to 7 times faster than
736 on ice sheets due to the constraints of conducting experiment in reasonable times, which requires
737 higher loads.

738

739 **Appendix B:** Strain rate minimum inferred via two kinds of constraints

740 To improve the reliability of inferred SRmins, two kinds of constraints were applied. First, the
741 SRmins from the -5°C and -18°C samples are calibrated using Glen's law $\dot{\varepsilon} = A\sigma^n$ with $n = 4.3$
742 (Li and Baker, 2022a). PC1-SRmin, PC2-SRmin, and PC3-SRmin indicate three possibilities of
743 the SRmins that are calculated from the 20 m, 40 m, and 60 m samples via the *only* SRmin
744 observed at a given temperature (Table 2). As an example, for the -5°C samples, there exist three
745 possibilities from three depths. 1) The SRmin observed from the 20 m sample in bold italic font is
746 used to calculate two other SRmins for the 40 m and 60 m samples in the italic font in the column
747 of PC1-SRmin. 2) In the same manner as in scenario 1), the SRmin observed from the 40 m
748 sample is calculated in the column of PC2-SRmin in the bold italic font, and the SRmin observed
749 from the 60 m sample is calculated in the column of PC3-SRmin in the bold italic font. 3) In the
750 same manner as in scenarios 1) and 2), the SRmin is calculated for the -18°C samples in turn
751 from three depths. Second, the SRMin of the -30°C samples is inferred on the basis of the range
752 of Q_c , i.e., from 44.8 kJ mol^{-1} (upper bound) to 113 kJ mol^{-1} (lower bound), using the Arrhenius
753 relation.

754 **Data availability**

755 The data supporting the conclusions in this study are available at <https://arcticdata.io/catalog>.

756

757 **Author contribution**

758 Y.L. and I.B. designed the experiments and Y.L. carried them out. Y.L. analyzed the data and
759 visualized the relevant results. Y.L. prepared the manuscript with contributions from all
760 co-authors (K.K. and I.B.).

761

762 **Competing interests**

763 At least one of the (co-)authors is a member of the editorial board of *The Cryosphere*.

764

765 **Acknowledgements**

766 This work was sponsored by the National Science Foundation under Arctic Natural Science Grant
767 No. 1743106. Y.L. gratefully acknowledges Ciao Fu for her great support and help in during the
768 COVID-19 pandemic. The authors wish to thank Chris Polashenski, Zoe Courville and Lauren B.
769 Farnsworth at USA-CRREL for their assistance with the storage of the firn cores. We also
770 acknowledge the use of facilities of the Ice Research Laboratory (Director-Erland Schulson) at
771 Dartmouth College. Finally, the authors thank Editor Nanna Bjørnholt Karlsson, Louis Védrine
772 and an anonymous reviewer for their constructive comments, which significantly improved the
773 quality of this manuscript.

774 **References:**

775 Adolph, A.C.C., Albert, M.R., 2014. Gas diffusivity and permeability through the firn column at
776 Summit, Greenland: measurements and comparison to microstructural properties. *T. Cryosph.*, 8, 319–328, doi:10.5194/tc-8-319- 2014.

777

778 Albert, M.R., Shultz, E.F. and Perron, F.E., 2000. Snow and firn permeability at Siple Dome,
779 Antarctica. *Ann. Glaciol.* 31, 353-356.

780 Alley, R.B., Clark, P.U., Huybrechts, P., Joughin, I., 2005. Ice-sheet and sea-level changes. *Sci.*
781 310(5747), 456-60. doi: 10.1126/science.1114613. PMID: 16239468.

782 Ambach, W., Eisner, H., 1985. Rheological properties of temperate firn. *Polarforschung*,
783 Bremerhaven, Alfred Wegener Institute for Polar and Marine Research & Germany Society
784 of Polar Research 55(2), 71–77. hdl:10013/epic.29564.d001.

785 Anderson, D.L., Benson, C.S., 1963. The densification and diagenesis of snow. In: Kingery, W.D.
786 (Ed.), *Ice and Snow*. Press, Cambridge, Massachusetts, M.I.T, pp. 391–411.

787 Arnaud, L., Gay, M., Barnola, J.M., Duval P., 1998. Imaging of firn and bubbly ice in coaxial
788 reflected light: a new technique for the characterization of these porous media. *J. Glaciol.*,
789 44(147), 326-332.

790 Ashby, M.F., Duval, P. 1985. The creep of polycrystalline ice. *Cold Reg. Sci. Technol.*, 11 (3),
791 285-300. doi:10.1016/0165-232X(85)90052-7.

792 Azuma, N., Higashi, A., 1984. Mechanical properties of Dye 3 Greenland deep ice cores. *Ann.*
793 *Glaciol.*

794 Baker, R.W., Gerberich, W.W., 1979. The effect of crystal size and dispersed-solid inclusions on
795 the activation energy for creep of ice. *J. Glaciol.*, 24(90), 179-194.

796 Barnes, P., Tabor, D., Walker, J.C.F., 1971. The friction and creep of polycrystalline ice. Proc. Roy.
797 Soc. Lond. A (324), 127-155.

798 Bartelt, P., Von Moos, M., 2000. Triaxial tests to determine a microstructure-based snow viscosity
799 law. Ann. Glaciol., 31, 457-462.

800 Bindschadler, R., King, M., Alley, R., Anandakrishnan, S., Padman, L., 2003. Tidally controlled
801 stick-slip discharge of a West Antarctic ice stream. Ann. Glaciol., 36, 157-162.

802 Brown, D.E., George, S.M., 1996. Surface and bulk diffusion of $H_2^{18}O$ on single-crystal $H_2^{16}O$ ice
803 multilayers. J. Phys. Chem. 100 (38) 15460-15469.

804 Budd, W.F., Jacka, T.H., 1989. A review of ice rheology for ice sheet modelling. Cold Reg. Sci.
805 Technol. 16(2), 107-144. doi: 10.1016/0165-232X(89)90014-1.

806 Burr, A., Ballot, C., Lhuissier, P., Martin^{erie}, P., Martin, C.L., Philip, A., 2018. Pore morphology
807 of polar firn around closure revealed by X-ray tomography. T. Cryosph., Copernicus, 12(7),
808 2481-2500. 10.5194/tc-12-2481-2018. hal-01864373.

809 Butkovich, T.R., Landauer, J.K., 1960. Creep of ice at low stresses. U.S. Snow, Ice and
810 Permafrost Research Establishment. Research Report 72.

811 Chandler, D., B. Hubbard, A. Hubbard, T. Murray, Rippin, D., 2008. Optimising ice flow law
812 parameters using borehole deformation measurements and numerical modelling. Geophys.
813 Res. Lett., 35, L12502.

814 Chen, M., Chen, Z.D., 1997. Effective stress laws for multi-porosity media. Appl. Math. Mech.,
815 20(11), 1207-1213.

816 Coleou, C., Lesaffre, B., Brzoska, J.B., Ludwig, W., Boller, E., 2001. Three-dimensional snow
817 images by X-ray microtomography. Ann. Glaciol., 32, 75-81.

818 Colgan, W., et al., 2023. Sixty years of ice form and flow at Camp Century, Greenland. *J. Glaciol.*,
819 69(276), 919–929.

820 Courville, Z., Horhold, M., Hopkins, M. and Albert, M., 2010. Lattice-Boltzmann modeling of the
821 air permeability of polar firn. *J. Geophys. Res., Earth Surface*, 115(F4).

822 Coussy, O., 2004. *Poromechanics*. John Wiley & Sons.

823 Cuffey, K.M., 2006. Manifestations of ice microphysical processes at the scale of whole ice sheets.
824 In: Knight, P. (Ed.), *Glacier Science and Environmental Change*. Blackwell Publishing, 290–
825 300.

826 Cuffey, K.M., Paterson, W.S.B., 2010. *The Physics of Glaciers*, 4th edited. Elsevier Inc.

827 Cuffey, K.M., Kavanaugh, J.L., 2011. How nonlinear is the creep deformation of polar ice? A new
828 field assessment. *Geol.*, 39(11), 1027–1030.

829 da Silva, M.R., Schroeder, C., Verbrugge, J.C., 2008. Unsaturated rock mechanics applied to a
830 low-porosity shale. *Eng. Geol.*, 97, 42–52.

831 Durham, W.B., Stern, L.A., 2001. Rheological properties of water ice applications to satellites of
832 the outer planets. *Annu. Rev. Earth Planet. Sci.* 29(1), 295–330.

833 Duval, P., 1981. Creep and fabrics of polycrystalline ice under shear and compression. *J. Glaciol.*
834 27, 129–140.

835 Duval, P. Ashby, M.F., Anderman, I., 1983. Rate-controlling processes in the creep of
836 polycrystalline ice. *The Journal of Physical Chemistry*, 87, 4066–4074.

837 Duval, P., Montagnat, M., 2002. Comment on ‘Superplastic deformation of ice: experimental
838 observations’ by D. L. Goldsby and D. L. Kohlstedt. *J. Geophys. Res.: Solid Earth*. 107(B4),
839 ECV 4-1–ECV 4-2. doi: 10.1029/2001JB000946.hal-01698732.

840 Ebinuma, T., Maeno, N., 1987. Particle rearrangement and dislocation creep in a snow
841 densification process. *J Phys.(Paris)*, 48, Colloq. C1, 263–269.

842 Ehlers, W., 2002. Foundations of multiphasic and porous materials. In Ehlers Wolfgang and
843 Bluhm J eds. *Porous Media— Theory, Experiments and Numerical Applications*. Berlin:
844 Springer, pp. 3–86.

845 Eichler, J., 7 others, 2017. Location and distribution of micro-inclusions in the EDML and NEEM
846 ice cores using optical microscopy and in situ Raman spectroscopy. *The Cryosphere*. 11(3),
847 1075–1090. doi: 10.5194/tc-11-1075-2017.

848 Faria, S.H., Weikusat, I., Azuma, N., 2014. The microstructure of polar ice. Part II: state of the art.
849 *J. Struct. Geol.* 61, 21–49. doi:10.1016/j.jsg.2013.11.003.

850 Fish, A.M. (1991) Creep and yield model of ice under combined stress. USA Cold Regions
851 Research and Engineering Laboratory, Special Report 91-31.

852 Flin, F., Brzoska, J.B., Lesaffer, B., Coleou, C., Pieritz, R.A., 2004. Three-dimensional geometric
853 measurements of snow microstructural evolution under isothermal conditions. *Ann. Glaciol.*,
854 38, 39-44.

855 Freitag, J., Dobrindt, U., Kipfstuhl, J., 2002. A new method for predicting transport properties of
856 polar firn with respect to gases on the pore-space scale, *Ann. Glaciol.*, 35, 538-544.

857 Frost, H.J., Ashby, M.F. 1982. *Deformation-mechanism maps: the plasticity and creep of metals
858 and ceramics*. Oxford: Pergamon Press.

859 Fujita, S., Hirabayashi, M., Goto-Azuma, K., Dallmayr, R., Satow, K., Zheng, J., Dahl-Jensen, D.,
860 2014. Densification of layered firn of the ice sheet at NEEM, *J. Glaciol.*, 60 (223), 905-921,
861 doi:10.3189/2014JoG14J006.

862 Gagliardini, O., Meyssonier, J., 2000. Simulation of the creep of ice with a self-consistent
863 anisotropic approach. *Comput. Mech.*, 25(5), 479-486.

864 Glen, J.W., 1955. The creep of polycrystalline ice, *Proceedings of the Royal Society A*, 228(1175),

865 519-538, doi.10.1098/rspa.1955.0066.

866 Goldsby, D.L., Kohlstedt, D.L., 1997. Grain boundary sliding in fine-grained ice I. *Scr. Mater.*
867 37(9), 1399–1406.

868 Goldsby, D.L., Kohlstedt, D.L., 2001. Superplastic deformation of ice: experimental observations,
869 *J. Geophys. Res.*, 106(B6), 11017-11030.

870 Goodman, D.J., Frost, H.J., Ashby, M.F., 1981. The plasticity of polycrystalline ice, *Philos. Mag.*,
871 A43 665–695.

872 Gow, A.J., 1969. On the rates of growth of grains and crystals in South Polar firn. *J. Glaciol.*, 8(53)
873 241-252.

874 Gray, W.G., Schrefler, B.A., 2007. Analysis of the solid stress tensor in multiphase porous media.
875 *Int. J. Numer. Anal. Methods Geomech.*, 31, 541–581.

876 Goujon, C., J.-M. Barnola, C. Ritz. 2003. Modeling the densification of polar firn including heat
877 diffusion: Application to close-off characteristics and gas isotopic fractionation for
878 Antarctica and Greenland sites, *J. Geophys. Res.*, 108(D24),
879 4792,doi:10.1029/2002JD003319.

880 Gubler, H., 1978. Determination of the mean number of bonds per snow grain and of the
881 dependence of the tensile strength of snow on stereological parameters. *J. Glaciol.*,
882 20(83),329-341.

883 Hammonds, K., Baker, I., 2016. The effects of Ca⁺⁺ on the strength of polycrystalline ice. *J.*
884 *Glaciol.* 62,1–9. doi: 10.1017/jog.2016.84.

885 Hammonds, K., Baker, I., 2018. The effects of H₂SO₄ on the mechanical behavior and
886 microstructural evolution of polycrystalline Ice. *J. Geophys. Res.: Solid Earth.* 123,1–22. doi:
887 10.1002/2017JF004335.

888 Hansen, B.L., Landauer, J.K., 1958. Some results of ice cap drill hole measurements. IASH Publ.
889 47 (Symposium at Chamonix 1958– Physics of the Movement of the Ice), 313–317.

890 Hansen, A.C., Brown, R.L., 1988. An internal state variable approach to constitutive theories for
891 granular materials with snow as an example. *Mech. Mater.*, 7(2), 109–119.

892 Higashi, A., Konimura, S., Mae, S., 1965. Plastic yielding in ice single crystals. *Jpn. J. Appl. Phys.*
893 4, 575–82.

894 Hildebrand, T., Ruegsegger, P. 1997. A new method for the model-independent assessment
895 of thickness in three-dimensional images. *J. Microsc.*, 185, 67–75.

896 Hobbs, P.V., 1974. *Ice Physics*, 1st edited. Oxford University Press Inc., New York.

897 Homer, D.R., Glen, J.W., 1978. The creep activation energies of ice. *J. Glaciol.*, 21(85), 429–444.

898 Hooke, R.L., Mellor, M., Budd, W.F., Glen, J.W., Higashi, A., Jacka, T.H., Jones, S.J., Lile, R.C.,
899 Martin, R.T., Meier, M.F., Russell-Head, D.S., Weertman, J., 1980. Mechanical properties of
900 polycrystalline ice: an assessment of current knowledge and priorities for research. *Cold Reg.
901 Sci. Technol.*, 3, 263–275.

902 Hooke, R.L., 1981. Flow law for polycrystalline ice in glaciers: comparison of theoretical
903 predictions, laboratory data, and field measurements. *Rev. Geophys. Space Phys.*, 19(4),
904 664–672.

905 Hooke, R.L., 2005. *Principles of Glacier Mechanics*. Cambridge: Cambridge University Press.

906 Horhold, M.W., 5 others, 2012. On the impact of impurities on the densification of polar firn.
907 *Earth Planet. Sci. Lett.* 325–326, 93–99. doi: 10.1016/j.epsl.2011.12.022

908 Hutter, K., Johnk, K., 2004. *Continuum Methods of Physical Modeling: Continuum Mechanics,
909 Dimensional Analysis, Turbulence*. Springer Science & Business Media.

910 Jacka, T.H. 1984. The time and strain required for development of minimum strain rates in ice.
911 *Cold Reg. Sci. Technol.*, 8 (3), 261–268. doi: 10.1016/0165-232X(84)90057-0.

912 Jacka, T.H., Li, J. 1994. The steady state crystal size of deforming ice. *Ann. Glacial.*, 20, 13–18.

913 Jacka, T.H., Li, J., 2000. Flow rates and crystal orientation fabrics in compression of
914 polycrystalline ice at low temperatures and stresses, Physics of Ice Core Records
915 International Symposium on Physics of Ice Core Records. Shikotsukohan, Hokkaido, Japan,
916 83-102.

917 Jonas, J.J., Muller, F., 1969. Deformation of ice under high internal shear stresses. *Can. J. Earth
918 Sci.* 6(4), 963–968. doi: 10.1139/e69-100.

919 Jumawan, A.B., 1972. An experimental study of self-diffusion in polycrystalline ice. *Diss. Abstr.
920 Int. B* 32, 5163–5164 (Abstract).

921 Kamb, B., 1961. The thermodynamic theory of nonhydrostatically stressed solids. *J. Geophys.
922 Res.* 66, 259–271.

923 Khalili, N., Geiser, F. Blight, G.E., 2004. Effective stress in un-saturated soils, a review with new
924 evidence. *Int. J. Geomech.*, 4(2), 115–126.

925 King, R.F., 1952. Dissertation, Cambridge.

926 Lade, P.V., Boer, R.V., 1997. The concept of effective stress for soil, concrete and rock. *Geotech.,
927* 47(1), 61–78.

928 Landauer, J.K., 1958. The creep of snow under combined stress. *Transactions of the society of
929 rheology II.* 175-194.

930 Li, J., Jacka, T.H., Budd, W.F., 1996. Deformation rates in combined compression and shear for
931 ice which is initially isotropic and after the development of strong anisotropy. *Ann. Glaciol.,
932* 23, 247-252.

933 Li, Y., Baker, I. 2021. Dynamic observations of the densification of polar firn under compression
934 using a micro-computed tomograph, *J. Geophys. Res., Earth Surface*, 126, e2021JF006290.
935 doi:org/10.1029/2021JF006290.

936 Li, Y. 2022. Critical values of the microstructural parameters at the first critical density of the
937 densification of polar firn. *Cold Reg. Sci. Technol.*, 198(2022), 10355.
938 doi:org/10.1016/j.coldregions.2022.103553.

939 Li, Y., Baker, I. 2022a. Observations of the creep of polar firn. *J. Glaciol.*, 68(268), 269–287.
940 doi.org/10.1017/jog.2021.91.

941 Li, Y., Baker, I. 2022b. Metamorphism observation and model of snow from Summit, Greenland
942 under both positive and negative temperature gradients in a Micro CT, *Hydrol. Processes*,
943 e14696. doi.10.1002/HYP.14696.

944 Li, Y. 2023b. Changes in grain size during the relaxation stage of viscoelastic firn, *Philos. Mag.*,
945 104(4), 239-259. doi.org/10.1080/14786435.2023.2296656.

946 Li, Y. Fu, C. Keegan, C. et al. 2023. Microstructural characterization of depth hoar and ice-crust
947 layers using a micro-CT, and hypothesis of ice-crust formation under a thunderstorm, *Hydrol.*
948 *Processes*, 37(12), e15060. doi.org/10.1002/hyp.15060.

949 Ligtenberg, S.R.M., Helsen, M.M., van den Broeke, M. R. 2011. An improved semi-empirical
950 model for the densification of Antarctic firn. *The Cryosphere*, 5, 809–819,
951 doi.org/10.5194/tc-5-809-2011.

952 Liu, K., Sun, R. & Daraio, C. 2022. Growth rules for irregular architected materials with
953 programmable properties. *Sci.*, 377(6609), 975-981.

954 Lundin, J.M., Stevens, C.M., Arthern, R., Buijzer, C., Orsi, A., Ligtenberg, S.R., et al. 2017. Firn
955 model intercomparison experiment (FirnMICE). *J. Glaciol.* 63(239), 401–422.
956 https://doi.org/10.1017/jog.2016.114.

957 Maeno, N., Ebinuma, T., 1983. Pressure sintering of ice and its implication to the densification of
958 snow at polar glaciers and ice sheets. *J. Phys. Chem.* 87, 4103–4110.

959 Mahajan, P. and R.L. Brown. 1993. A microstructure-based constitutive law for snow. *Ann.*

960 Glaciol., 18, 287–294.

961 McCarthy, C., Savage, H., Nettles, M., 2017. Temperature dependence of ice-on-rock friction at
962 realistic glacier conditions. *J. Glaciol.*, 63(241), 595–606.

963 Mellor, M., Smith, J.H., 1966. Creep of snow and ice, CRREL Res. Rep. 220.

964 Mellor, M., Testa, R., 1969. Effect of temperature on the creep of ice. *J. Glaciol.*, 8(52), 131–145.

965 Mellor, M., 1975. A review of basic snow mechanics. *Int. Assoc. Hydrol. Sci.* 114, 251–291.

966 Meussen, B., Mahrenholtz, O., Oerter, H., 1999. Creep of polar firn. *Cold Reg. Sci. Technol.* 29,
967 177–200. doi: 10.1016/S0165-232X(99)00018-X

968 Millstein, J.D., Minchew, B.M., Pegler, S.S., 2022. Ice viscosity is more sensitive to stress than
969 commonly assumed. *Commun. Earth Environ.*, 3, 57.

970 Nasello, O.B., Di Prinzio, C.L., Guzman, P.G., 2005. Temperature dependence of “pure” ice grain
971 boundary mobility, *Acta Mater.*, 53(18) 4863–4869, doi: 10.1016/j.actamat.2005.06.022.

972 Nuth, M., Laloui, L., 2008. Effective stress concept in unsaturated soils: clarification and
973 validation of a unified framework. *Int. J. Numer. Anal. Methods Geomech.*, 32, 771–801.

974 Ogunmolasuyi, A., Murdza, A., Baker, I. 2023. The onset of recrystallization in polar firn.
975 *Geophys. Res. Lett.*, 50, e2023GL103435. doi.org/10.1029/2023GL103435.

976 Paterson, W.S.B., Savage, J.C., 1963. Measurements on Athabasca Glacier relating to the flow
977 law of ice. *J. Geophys. Res.*, 68:4537–43.

978 Paterson, W.S.B., 1977. Secondary and tertiary creep of glacier ice as measured by borehole
979 closure rates, *Rev. Geophys. Space Phys.*, 15, 47–55.

980 Perutz, M.F., Seligman, G., 1939. A crystallographic investigation of glacier structure and the
981 mechanism of glacier flow. *Proc. Roy. Soc. London A* 172, 335–360.

982 Petrenko, V.F., Whitworth, R.W., 1999. *Physics of Ice*. Oxford: Oxford University Press.

983 Pimienta, P., Duval, P., 1987. Rate controlling processes in the creep of polar glacier ice. *Journal*
984 *de Physique*, 48, 243-248.

985 Raymond, C.F., 1973. Inversion of flow measurements for stress and rheological parameters inva
986 valley glacier. *J. Glaciol.* 12, 19–44.

987 Salamatin, A.N., Lipenkov, V.Y., Barnola, J.M., Hori, A., Duval, P., Hondoh, T. 2009. Snow/firn
988 densification in polar ice sheets. In: Hondoh, T. (Ed.), III. Firn densification, close-off and
989 chronology, 195-222, Hokkaido University Press.

990 Salm, B., 1982. Mechanical properties of snow. *Rev. Geophys. Space Phys.*, 20(N1), 1–19.

991 Scapozza, C., Bartelt, P.A., 2003. The influence of temperature on the small-strain viscous
992 deformation mechanics of snow: a comparison with polycrystalline ice. *Ann. Glaciol.*, 37,
993 90–96.

994 Schleef, S., Lowe, H., Schneebeli, M., 2014. Influence of stress, temperature and crystal
995 morphology on isothermal densification and specific surface area decrease of new snow. *T.*
996 *Cryosphy.*, 8, 1825-1838.

997 Schwander, J., Sowers, T., Barnola, J.-M., Blunier, T., Fuchs, A., Malaize, B. 1997. Age scale of
998 the air in the summit ice: Implication for glacial-interglacial temperature change, *J. Geophys.*
999 *Res.*, 102(D16), 19483–19493, doi.org/10.1029/97JD01309.

1000 Simonsen SB, Stenseng L, Adalgeirsdottir G, Fausto RS, Hvidberg CS, Lucas-Picher P. 2013.
1001 Assessing a multilayered dynamic firn-compaction model for Greenland using ASIRAS
1002 radar measurements, *J. Glaciol.*, 59(215), 545–558, doi.org/10.3189/2013JoG12J158.

1003 Sinha, N.K., 1978. Short-term rheology of polycrystalline ice. *J. Glaciol.*, 21(85) 457-472.

1004 Steinemann, S., 1954. Flow and recrystallisation of ice. *Proc. Int. Assoc. Hydrol. Sci.* 39, 449–
1005 462.

1006 Song, M., Baker, I., Cole, D.M., 2005. The effect of particles on dynamic recrystallization and

1007 fabric development of granular ice during creep. *J. Glaciol.* 51(173), 377–382. doi:
1008 10.3189/172756505781829287.

1009 Song, M., Cole, D.M., Baker, I., 2006a. Investigation of Newtonian creep in polycrystalline ice.
1010 *Philos. Mag. Lett.* 86(12), 763–771. doi: 10.1080/09500830601023787.

1011 Song, M., Cole, D.M., Baker, I. 2006b. An investigation of the effects of particles on creep of
1012 polycrystalline ice. *Scr. Mater.* 55, 91–94. doi: 10.1016/j.scriptamat.2006.03.029.

1013 Song, M., Baker, I., Cole, D.M., 2008. The effect of particles on creep rate and microstructures of
1014 granular ice. *J. Glaciol.* 54(186), 533–537. doi:10.3189/002214308785836959.

1015 Srivastava, P.K., Mahajan, P., Satyawali, P.K., 2010. A constitutive law for the densification of
1016 polar firn. *Cold Reg. Sci. Technol.*, 60(2), 133-138.

1017 Theile, T., Lowe, H., Theile, T.C., Schneebeli, M., 2011. Simulating creep of snow based on
1018 microstructure and the anisotropic deformation of ice. *Acta Mater.* 59, 7104–7113. doi:
1019 10.1016/j.actamat.2011.07.065.

1020 Thomas, R.H., MacAyeal, D.R., Bentley, C.R., Clapp, J.L., 1980. The creep of ice, geothermal
1021 heat flow, and Roosevelt Island, Antarctica. *J. Glaciol.* 25, 47–60.

1022 Treverrow, A., Budd, W.F., Jacka, T.H., Warner, R.C., 2012. The tertiary creep of polycrystalline
1023 ice: experimental evidence for stress-dependent levels of strain-rate enhancement. *J. Glaciol.*
1024 58(208), 301–314. doi: 10.3189/2012JoG11J149.

1025 Vedrine, L., Hagenmuller, P., Gelebart, L., Montagnat, M., Lowe, H. (2025). Sensitivity of the
1026 viscoplasticity of polycrystals to porosity and pore-to-crystal size ratio. *Acta Materialia*, 301,
1027 121507. doi.org/10.1016/j.actamat.2025.121507.

1028 Vickers, W., Greenfield, P., 1968. The high temperature creep properties of compacted
1029 magnesium powder. *Journal of Nuclear Materials*, 27(1), 73-79.

1030 Wang, X., Baker, I., 2013. Observation of the Microstructural Evolution of Snow under Uniaxial
1031 Compression using X-ray Computed Micro-tomography, *J. Geophys. Res.*, 118, 1-12,
1032 doi.org/10.1002/2013JD020352.

1033 Weertman, J., 1983. Creep deformation of ice. *Annual Review Earth Planet Science*, 11, 215–240.

1034 Weertman, J., 1985. Unsolved problems of creep. *Nat.* 314(6008), 227.

1035 Wiese, M., Schneebeli, M., 2017. Snowbreeder 5: a Micro-CT device for measuring the
1036 snow-microstructure evolution under the simultaneous influence of a temperature gradient
1037 and compaction. *J. Glaciol.*, 63(238), 355–360, doi: 10.1017/jog.2016.143.